Yoon *et al. Energy Mater* 2024;4:400063
DOI: 10.20517/energymater.2023.146

Energy Materials

Review

Open Access

Check for updates

Recent advances in Sb-based anodes for Li/Na/K-ion batteries and all-solid-state Li-ion batteries

Jeong-Myeong Yoon[1,2,#], Deok-Gyu Kim[1,2,#], Do-Hyeon Kim[1,2], Young-Han Lee[1,2], Cheol-Min Park[1,2,*]

[1]School of Materials Science and Engineering, Kumoh National Institute of Technology, Gyeongbuk 39177, Republic of Korea.
[2]Department of Energy Engineering Convergence, Kumoh National Institute of Technology, Gyeongbuk 39177, Republic of Korea.
[#]Authors contributed equally.

Correspondence to: Prof. Cheol-Min Park, School of Materials Science and Engineering, Kumoh National Institute of Technology, 61 Daehak-ro, Gumi, Gyeongbuk 39177, Republic of Korea; Department of Energy Engineering Convergence, Kumoh National Institute of Technology, 61 Daehak-ro, Gumi, Gyeongbuk 39177, Republic of Korea. E-mail: cmpark@kumoh.ac.kr

How to cite this article: Yoon JM, Kim DG, Kim DH, Lee YH, Park CM. Recent advances in Sb-based anodes for Li/Na/K-ion batteries and all-solid-state Li-ion batteries. *Energy Mater* 2024;4:400063. https://dx.doi.org/10.20517/energymater.2023.146

Received: 31 Dec 2023 **First Decision:** 7 Apr 2024 **Revised:** 18 May 2024 **Accepted:** 17 Jun 2024 **Published:** 26 Jun 2024

Academic Editor: Wei Tang **Copy Editor:** Fangyuan Liu **Production Editor:** Fangyuan Liu

Abstract

In recent decades, lithium-ion batteries (LIBs) have emerged as a primary focus in the energy-storage field owing to their superior energy and power densities. However, concerns regarding the depletion of non-abundant lithium resources have prompted the exploration and development of emerging energy-storage technologies, such as sodium- (SIBs) and potassium-ion batteries (PIBs). In addition, all-solid-state LIBs (ASSLIBs) have been developed to address the issues of flammability and explosiveness associated with liquid electrolytes. Among the various alloy-based anodes, antimony (Sb) anodes exhibit high energy densities owing to their high theoretical volumetric capacities that are attributable to their high densities. However, Sb anodes exhibit poor cyclabilities owing to excessive volume changes during cycling. To mitigate this issue, researchers have investigated the use of diverse solutions, including solid electrolyte interface control, structural control, and composite/alloy formation. Herein, we review and summarize Sb-based anode materials for LIBs, SIBs, PIBs, and ASSLIBs developed over the past five years (2018-present), focusing on their reaction mechanisms and multiple approaches used to achieve optimal electrochemical performance. We anticipate that this review will provide a comprehensive database of Sb-based anodes for LIBs, SIBs, PIBs, and ASSLIBs, thereby advancing relevant studies in the energy-storage-systems field.

Keywords: Battery, Li-ion battery, Na-ion battery, Sb-based anode, K-ion battery, all-solid-state battery, anode

INTRODUCTION

The increasing demand for sustainable energy storage has driven research into high-performance battery technologies[1-5]. Lithium-ion batteries (LIBs) currently dominate the secondary battery market but are anticipated to face limitations in the near future owing to unevenly distributed Li reserves and the depletion of Li resources. To address these concerns, new energy storage system (ESS) technologies, such as sodium- (SIBs)[6-10] and potassium-ion batteries (PIBs)[10-16], have emerged as secondary battery systems that utilize Na and K as charge carriers. Because Na and K belong to the same elemental group as Li, they undergo electrochemical reactions similar to Li (-3.04 *vs.* Li^+/Li). Consequently, they offer advantages in terms of adoption in LIB systems, including electrode material selection and analytical methods. Additionally, Na and K are abundantly available, inexpensive, and have standard electrode potentials similar to Li (Na: -2.71 *vs.* Na^+/Na, K: -2.93 *vs.* K^+/K). However, owing to safety concerns regarding liquid-electrolyte-based systems[17-19], all-solid-state LIBs (ASSLIBs) are regarded as next-generation battery technologies owing to the utilization of solid electrolytes, which are more mechanically strong and non-flammable compared to typical carbonate-based liquid electrolytes. ASSLIBs can suppress thermal runaway and deliver higher energy densities than LIBs by eliminating the need for separators and replacing fire-related safety devices[20,21].

Enhancing high-performance anode materials remains a critical challenge. Carbonaceous anode materials (mainly graphite) have long been used in LIBs owing to their cycling stabilities and low costs[17]. However, high-performance anodes need to overcome the inherent limitations of the low theoretical capacities and sluggish rate capabilities of carbonaceous anode materials. Similarly, high-performance anode materials for SIBs and PIBs are also urgently needed[22-24]. Hard carbon is the preferred SIB anode material because the interlayer spacing of graphite is too narrow to accommodate Na ions. However, hard carbon has a limited reversible capacity with a poor initial Coulombic efficiency (ICE). Although various carbonaceous anode materials can be used in PIBs, they exhibit low reversible capacities (279 mAh g^{-1}, KC_8). Similarly, during the initial stages of ASSLIB research, a solid electrolyte with a high mechanical strength physically inhibited the growth of Li dendrites, thereby facilitating the direct utilization of lithium metal. However, recent studies have found that the direct use of lithium metal results in self-destructive properties[19,20] that also promote the decomposition of the solid electrolyte at the interface, leading to the growth of Li dendrites. Furthermore, graphite anodes also accelerate solid-electrolyte deterioration due to their low reaction potentials (0-0.2 V *vs.* Li^+/Li) and high electrical conductivities (~10^3 S/m)[25,26]. Therefore, research into high-performance anode materials applicable to LIBs, SIBs, PIBs, and ASSLIBs with high capacities, long-term cycling stabilities, fast rate capabilities, and that do not form dendrites is required.

Antimony (Sb) is a promising alternative high-performance next-generation anode material candidate that simultaneously meets the aforementioned requirements for LIBs, SIBs, PIBs, and ASSLIBs. Figure 1 shows that an Sb anode exhibits the same high theoretical capacity of 660 mAh g^{-1} [Table 1 and Figure 1A] in alkali metal-ion batteries (AIBs)[9-16,27-39]. In particular, the Sb anode offers a high theoretical volumetric capacity (Table 1 and Figure 1B, 4,420 mA h cm^{-3})[27-31], which is attributable to the high density of Sb (6.70 g cm^{-3} at ambient temperature). Although the theoretical capacity of Sb is high, Sb anodes are poorly cyclable owing to excessive volume change experienced during cycling (Table 1 and Figure 1C; Li_3Sb: 134%, Na_3Sb: 291%, and K_3Sb: 406%). To address the issue of Sb anodes, researchers have explored various strategies based on a comprehensive understanding of their electrochemical reaction mechanisms in AIBs and ASSLIBs. Among numerous studies and strategies, this review focuses on three main strategies for improving the performance of Sb-based anodes. First, solid electrolyte interface (SEI) layer control is a strategy for optimizing the construction and composition of the SEI layer that develops on the electrode surface during cell operation. An ideal SEI layer is chemically stable, ion-conductive, and inhibits excessive electrolyte decomposition,

Table 1. Electrochemical properties of graphite, Si, Sn, and Sb anodes for LIBs, SIBs, and PIBs

Anode material	Theoretically fully discharged phase	Density (g cm^{-3})	Molar mass (g mol^{-1})	Molar volume (cm^3 mol^{-1})	Theoretical capacity		Volume change (%)
					gravimetric (mAh g^{-1})	volumetric (mAh cm^{-3})	
Graphite (C)	LiC_6	2.20	79.0	36	372	841	12.1
	NaC_{64}	1.85	791.6	428	35	79	25.8
	KC_8	1.95	135.2	69	279	631	63.1
Silicon (Si)	$Li_{4.4}Si$	1.18	58.6	50	4,199	9,786	312.1
	NaSi	1.76	51.1	29	954	2,223	140.8
	KSi	1.76	67.2	38	954	2,223	216.7
Tin (Sn)	$Li_{4.4}Sn$	1.92	149.2	78	993	7,259	378.7
	$Na_{3.75}Sn$	2.38	204.9	86	847	6,192	430.2
	KSn	3.46	157.8	46	226	1,652	180.8
Antimony (Sb)	Li_3Sb	3.35	142.6	43	660	4,420	134.1
	Na_3Sb	2.69	190.7	71	660	4,420	290.7
	K_3Sb	2.60	239.1	92	660	4,420	405.7

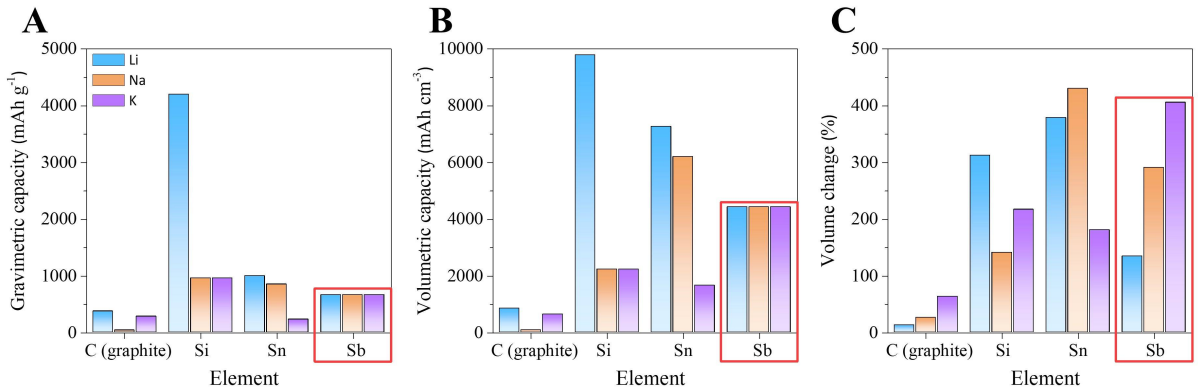

Figure 1. Comparing various anode materials (graphite (C), Si, Sn, and Sb) for LIBs, SIBs, and PIBs. (A) Theoretical gravimetric capacities. (B) Theoretical volumetric capacities. (C) Volume changes during electrochemical reactions. Parameter values were calculated for theoretically fully discharged phases (C: LiC_6, NaC_{64}, KC_8; Si: $Li_{4.4}Si$, NaSi, KSi; Sn: $Li_{4.4}Sn$, $Na_{3.75}Sn$, KSn; Sb: Li_3Sb, Na_3Sb, K_3Sb).

thereby enhancing cycling stability[40,41]. Second, structural control strategy involves tailoring the morphology and nanostructure of the Sb material. Techniques such as creating porous structures, nanoparticles, or nanowires can improve the electrolyte accessibility to the active material and accommodate volume change during the electrochemical reaction, thereby improving the rate capability and reducing capacity degradation[42-44]. Third, composite/alloy formation strategy provides high battery performance by incorporating other elements that can improve the electrical conductivity of Sb anodes and enhance their mechanical stability by suppressing volume change[45-54]. Other improvement strategies, including using protective layers[55,56] and highly conductive additives[57,58], are also available. Unfortunately, the abovementioned improvements only provide temporary performance enhancements, and their abuse can result in undesirable side reactions that degrade performance. On the other hand, binder optimization undeniably improves performance by enhancing the mechanical strength of the active material and its adhesion to the current collector[59]. However, the binder does not directly participate in electrochemical reactions; therefore, the three key-point strategies discussed above are directly related to the electrochemical reaction and significantly affect performance improvement. This review presents recent breakthroughs in Sb-based anodes for AIBs and ASSLIBs reported over the past five years (2018-2023).

REACTION MECHANISM

Sb anodes undergo alloying/dealloying with alkali metal ions, especially Li^+, Na^+, and K^+, to form Li_3Sb, Na_3Sb, and K_3Sb during charging and discharging. In addition, Sb has a unique puckered structure, and its interlayer space effectively accommodates the insertion of alkali metal ions. The reported electrochemical reaction mechanism of the Sb anode during discharging and charging in each system (LIBs, SIBs, PIBs, and ASSLIBs) is summarized below.

Sb-anode reaction mechanism in LIBs

Various studies have examined the electrochemical reaction mechanisms associated with Sb anodes in LIBs[60-62]. Park *et al.* demonstrated the reaction mechanism of an Sb anode using *ex-situ* X-ray diffraction (XRD)[60]. During discharging (lithiation), rhombohedral Sb alloys with Li form an intermediate crystalline hexagonal Li_2Sb phase and then transform into a fully discharged cubic Li_3Sb phase. In contrast, during charging (delithiation), cubic Li_3Sb is directly converted into rhombohedral Sb without involving an intermediate phase. Shin *et al.* demonstrated the same electrochemical reaction mechanism using *in-situ* time-domain thermoreflectance analysis[61]. The asymmetric behavior of the Sb anode during discharging and charging was also elucidated by Chang *et al.* using first-principles calculations and nuclear magnetic resonance (NMR) spectroscopy[62]. These researchers insisted that the higher nucleation driving force associated with Sb results in a single-step reaction pathway in which Li_3Sb is directly recovered to Sb without forming a thermodynamically stable Li_2Sb intermediate phase during the charging process. Therefore, the suggested reaction mechanism for the Sb anode in LIBs during discharging/charging is summarized by equations (1) and (2), along with the crystallographic schematic shown in Figure 2.

During discharging:

$$\text{Sb (Rhombohedral)} \rightarrow \text{Li}_2\text{Sb (Hexagonal)} \rightarrow \text{Li}_3\text{Sb (Cubic)} \quad (1)$$

During charging

$$\text{Li}_3\text{Sb (Cubic)} \rightarrow \text{Sb (Rhombohedral)} \quad (2)$$

Sb-anode reaction mechanism in SIBs

The Sb anode in SIBs exhibits a symmetric reaction mechanism during discharging (sodiation) and charging (desodiation), unlike the behavior observed in LIBs[63-67]. Darwiche *et al.* reported that rhombohedral Sb alloyed with Na forms an amorphous intermediate Na_xSb ($x < 3$) phase during the discharge reaction[63] owing to the sluggish kinetics associated with the crystallization of NaSb into the monoclinic structure. Subsequently, amorphous Na_xSb is transformed into hexagonal Na_3Sb. Conversely, during charging, Na_3Sb is transformed back into amorphous Na_xSb, which is recovered as rhombohedral Sb. Although XRD clearly identified Na_3Sb, the Na_xSb phase was not detected owing to its amorphous nature. Recent first-principles calculations performed by Caputo and Yu *et al.* demonstrated that the Na_xSb phase corresponds to monoclinic NaSb, which is the most thermodynamically stable phase[64,65]. This theoretical prediction was further supported by the experimental results, which are demonstrated using extended X-ray absorption fine structure analysis by Yu *et al.*, and *in-situ* XRD by Tian *et al.*[66,67]. Therefore, the suggested reaction mechanism for the Sb anode in SIBs during discharging/charging is summarized by equations (3) and (4), along with the crystallographic schematic shown in Figure 3.

During discharging:

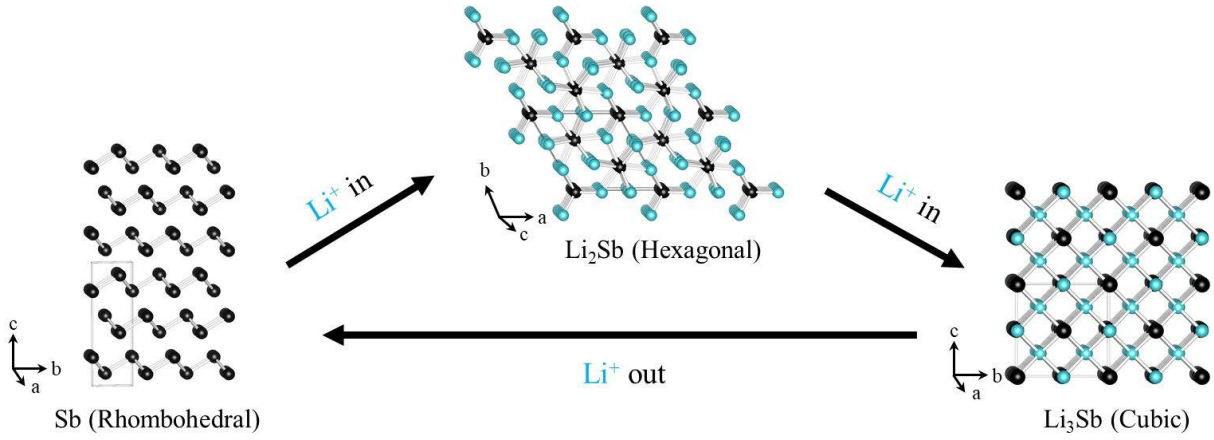

Figure 2. Crystallographic schematic of the Li-ion reaction pathway for an Sb anode in LIBs.

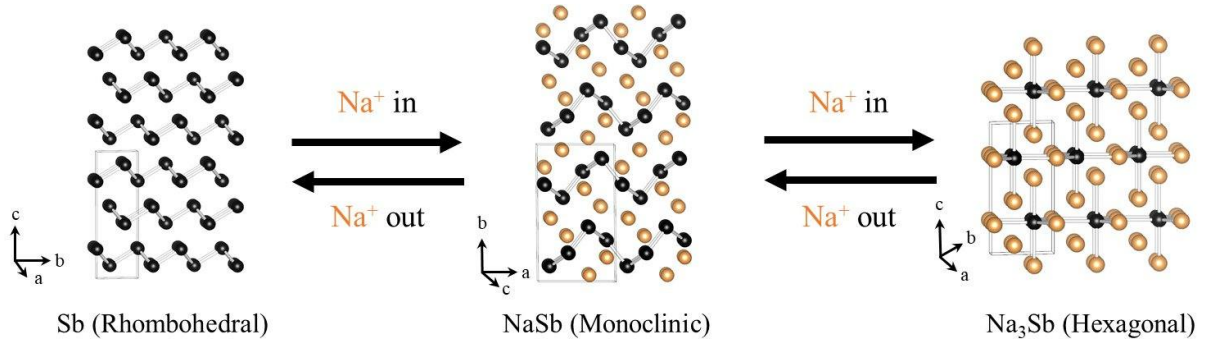

Figure 3. Crystallographic schematic of the Na-ion reaction pathway for an Sb anode in SIBs.

$$\text{Sb (Rhombohedral)} \rightarrow \text{NaSb (Monoclinic)} \rightarrow \text{Na}_3\text{Sb (Hexagonal)} \quad (3)$$

During charging:

$$\text{Na}_3\text{Sb (Hexagonal)} \rightarrow \text{NaSb (Monoclinic)} \rightarrow \text{Sb (Rhombohedral)} \quad (4)$$

Sb-anode reaction mechanism in PIBs

Several studies have reported the K-ion reaction pathway for an Sb anode in PIBs during discharging (potassiation) and charging (depotassiation)[68-70]. The Sb reaction mechanism was investigated by Gabaudan *et al.* using operando XRD[68]. During discharging, rhombohedral Sb is alloyed with K to form an intermediate amorphous K_xSb ($x < 3$) phase, which then transforms into cubic K_3Sb and hexagonal K_3Sb. In contrast, during charging, both cubic and hexagonal K_3Sb transform back into amorphous K_xSb, which is then recovered as rhombohedral Sb. To identify the amorphous K_xSb phases, Zheng *et al.* conducted first-principles calculations based on the K-Sb binary phase diagram and cyclic voltammetry[69], while Ko *et al.* performed first-principles calculations along with *in-situ* XRD[70]. These studies demonstrated that the KSb phase is the most stable among the various intermediate K_xSb phases (KSb_2, KSb, and K_5Sb_4); however, all the three phases are difficult to crystallize due to their low phase stabilities. Notably, *in-situ* XRD revealed only rhombohedral Sb and cubic K_3Sb, without any peaks corresponding to K_xSb observed. However, the identification of the K_xSb phase remains uncertain. Additionally, although the hexagonal K_3Sb phase is thermodynamically stable under ambient conditions, Sb is transformed into cubic K_3Sb during

electrochemical testing. The proposed reaction mechanism for the Sb anode in PIBs during discharging and charging is summarized by equations (5) and (6), along with the crystallographic schematic shown in Figure 4.

During discharging:

$$\text{Sb (Rhombohedral)} \rightarrow K_xSb \rightarrow K_3Sb \text{ (Cubic)} \quad (5)$$

During charging:

$$K_3Sb \text{ (Cubic)} \rightarrow K_xSb \rightarrow \text{Sb (Rhombohedral)} \quad (6)$$

RECENT ADVANCES IN ANTIMONY-BASED ANODES

Owing to its high theoretical gravimetric and volumetric capacities, Sb exhibits significant potential as an anode material for LIBs, SIBs, and PIBs [Figure 1A and B]. However, the alloying reaction with Li induces substantial volume changes and internal stresses in the Sb particles [Figure 1C], which leads to pulverization. Consequently, pulverized Sb particles inevitably form an additional SEI layer through further reactions with the electrolyte during repeated cycling, resulting in irreversible side reactions[55,71]. Therefore, researchers have proposed various strategies to address the challenges associated with excessive volume changes, including SEI layer control, structural control, and composite/alloy formation, to achieve highly stable cycling and rate capabilities [Figure 5]. This section systematically presents recent research progress focused on overcoming such drawbacks from the perspectives of SEI layer control, structural control, and composite/alloy formation.

Sb-based anodes for LIBs

Sb is considered a competitive anode owing to its abundance, metallic properties, high theoretical capacity (Li_3Sb: 660 mAh g^{-1}), and moderate potential (0.5-0.8 V *vs.* Li^+/Li). However, Sb-based anodes undergo excessive volume changes (~134%), and the continuous formation and destruction of the SEI layer result in capacity degradation and electrolyte starvation. To address these issues, recent advances in SEI layer control, structural control, and composite/alloy formation of Sb-based anode for LIB applications have been reported.

Researchers have explored the use of various solvents and salts to improve the SEI layer properties of Sb-based anodes[72-74]. Bian *et al.* reported incorporating fluoroethylene carbonate (FEC) into a propylene carbonate (PC) electrolyte in the LIB system[72]. This approach facilitates the construction of a stable SEI layer on a microsized Sb anode during Li cycling [Figure 6A]. Analysis using first-principles calculations, X-ray photoelectron spectroscopy (XPS), and scanning electron microscopy (SEM) revealed that FEC has a lower LUMO (the lowest unoccupied molecular orbital) energy level (-0.11 eV) compared to PC (0 eV). The FEC additive decomposes ahead of PC to create a LiF-rich SEI layer on the Sb surface that suppresses continuous electrolyte decomposition and contributes to facile ion/electron transfer and structural stability during repeated cycling. Furthermore, the microsized Sb exhibited a high reversible capacity of 575 mAh g^{-1} and a high ICE of 81% after 70 cycles at a high current rate of 5 A g^{-1}. Sun *et al.* developed a non-flammable triethyl phosphate (TEP)/1,1,2,2-tetrafluoroethyl-2,2,3,3-tetrafluoropropyl ether (HFE) electrolyte to improve the stability of a bulk Sb anode [Figure 6B][73]. The solvation structures formed by lithium bis(fluoroslufonyl)imide (LiFSI)-TEP/HFE exhibited distinct dipole-dipole interactions that provided excellent kinetics and compatibility with the anode material. Therefore, the bulk Sb anode showed a highly reversible capacity of 604 mAh g^{-1} with a substantial capacity retention of 92% after 100 cycles at a current

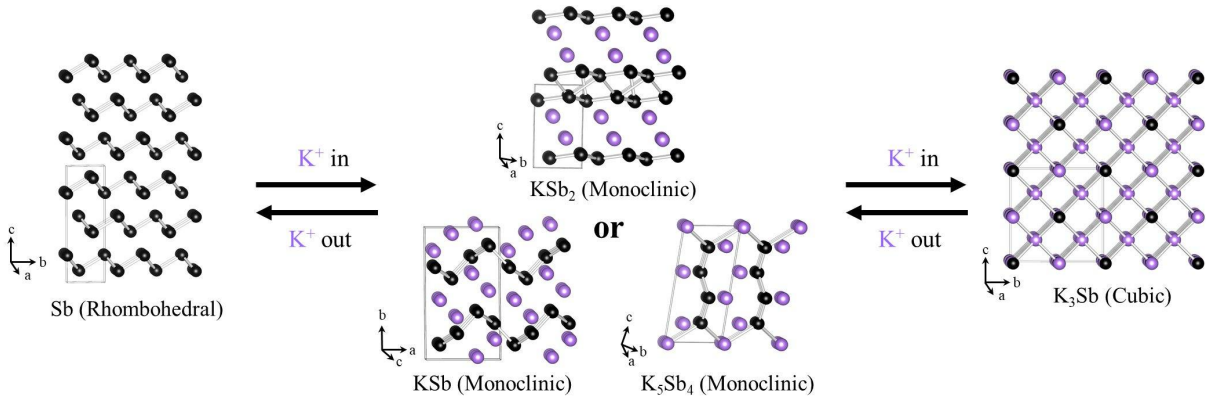

Figure 4. Crystallographic schematic of the K-ion reaction pathway for an Sb anode in PIBs.

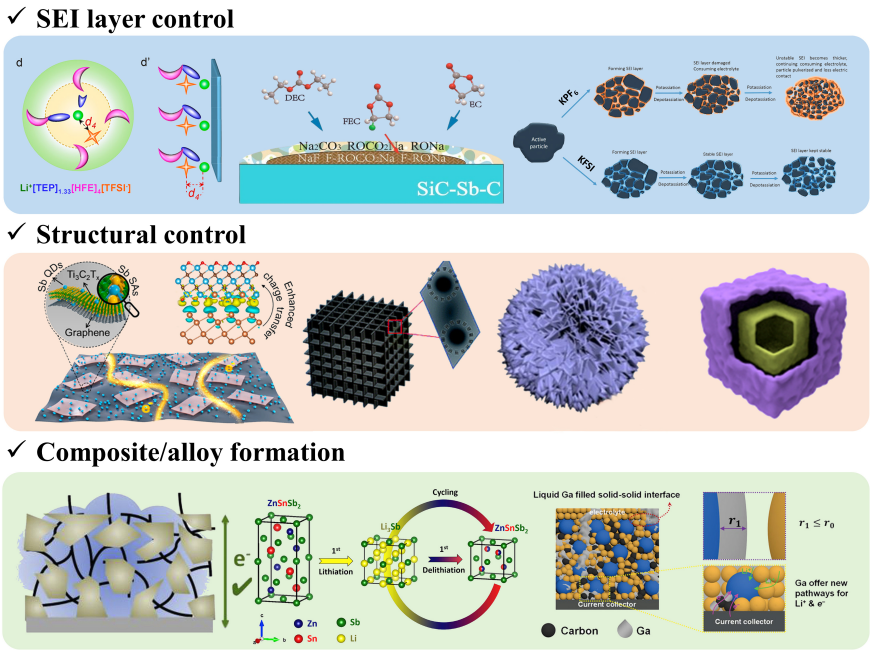

Figure 5. Schematic showing various strategies employed to engineer Sb anodes for LIBs, SIBs, PIBs, and ASSLIBs.

rate of 500 mA g^{-1} when evaluated using 1.2 M LiFSI in TEP/HFE as the electrolyte. Cai *et al.* investigated the effect of $LiNO_3$, as an electrolyte additive, on ether-based electrolytes with the aim of stabilizing the Sb anode [Figure 6C][74]. To determine the effectiveness of the $LiNO_3$ electrolyte additive, the Sb anode and SEI layers on the particles were investigated using SEM, XPS, and electrochemical impedance spectroscopy (EIS), which revealed that NO^{3-} weakens the Li^+-DME (dimethoxyethane) interaction, resulting in Li^+-2DME-NO^{3-} located away from the surface of the Sb anode, thereby suppressing electrolyte decomposition. The $LiNO_3$ additive decreased the strength of the interaction between the Li ion and the DME solvent molecule and affected the Li-ion solvation/desolvation process. The pristine Sb anode exhibited an ICE of 82.5% and a reversible capacity of 624 mAh g^{-1} after 100 cycles at a current density of 66 mA g^{-1}. Furthermore, a full cell with a $LiNi_{0.6}Co_{0.2}Mn_{0.2}O_2$ (NCM622) cathode maintained a capacity of 140.8 mAh g^{-1} over 100 cycles without any apparent capacity loss. Therefore, selecting appropriate solvents and salts is critical for establishing stable SEI layers on Sb-based anodes in LIBs.

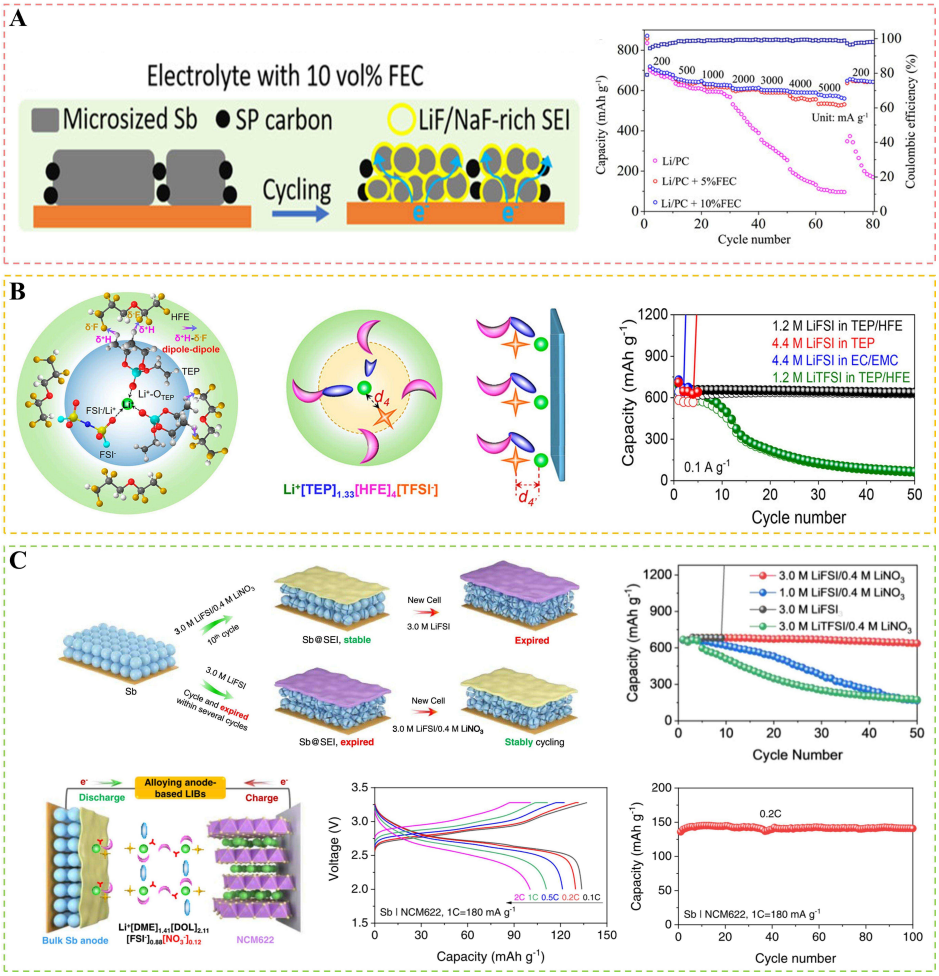

Figure 6. (A) Schematic illustration and rate capabilities of microsized Sb using FEC additives[72]. (B) Schematic illustration and cyclabilities of bulk Sb using LiFSI-based electrolytes[73]. (C) Schematic illustration, rate capabilities, and cyclabilities of a pristine Sb anode using $LiNO_3$ additives[74]. This figure is reproduced with permission from Bian *et al.*[72], Sun *et al.*[73], and Cai *et al.*[74].

Porous and multidimensional structural materials with high surface areas have been proposed as high-performance Sb-based anodes for LIBs[75-77]. These structured Sb anodes effectively accommodate volume changes during cycling. Liu *et al.* synthesized spherical Sb/C composites to address volume change during the charge/discharge process [Figure 7A][75]. The mesoporous Sb/C structure provided more Li-active sites and faster kinetics, which were attributed to the higher surface area that effectively accommodated volume changes due to the buffer effect. Consequently, the spherical Sb/C composite anode exhibited an impressive ICE of 86.7% and maintained a reversible capacity of 590 mAh g^{-1} after 80 cycles at a current rate of 100 mA g^{-1}. Schulze *et al.* prepared an Sb/carbon nanotube (CNT) composite film anode without any conductive additive or binder to improve mechanical/electrical connectivity [Figure 7B][76]. SEM revealed that the initial morphology of the prepared film consisted of a porous bead-on-string structure. The film thickness increased by 500% during more than 100 cycles owing to volume expansion and continuous SEI layer formation. However, the Sb/CNT composite film retained mechanical and electrical connections without delamination and exhibited a stable cycling performance of 340 mAh g^{-1} after 100 cycles at a current rate of 100 mA g^{-1} without any binder or conductive additives. Luo *et al.* fabricated a durable LIB anode using Sb/N-C with a unique nanorod-in-nanotube structure [Figure 7C][77] with an internal void capable of accommodating volume changes upon cycling. In addition, the combination of N-doped 1D conductive

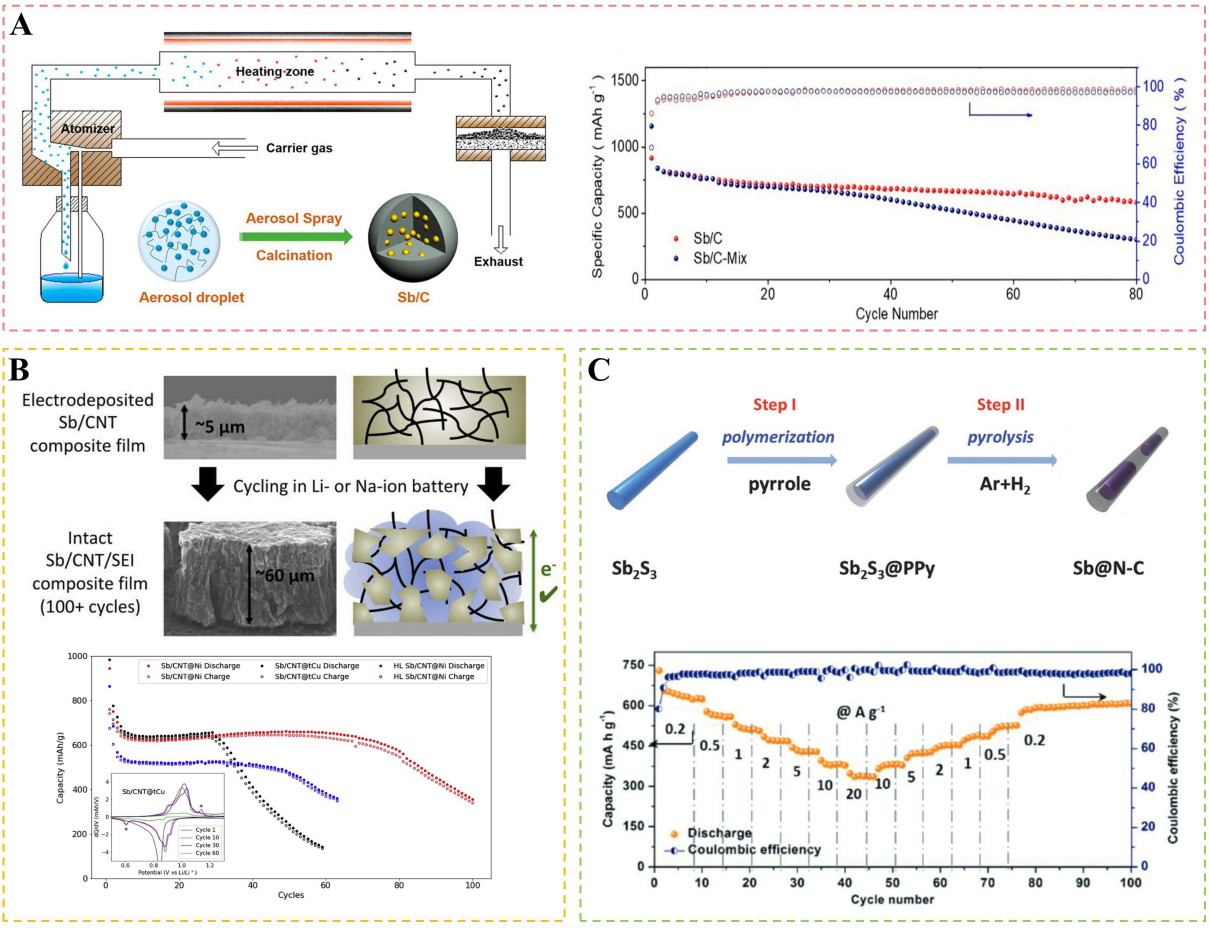

Figure 7. (A) Schematic illustration and cyclabilities of spherical Sb/C composite anodes[75]. (B) Schematic illustration and cyclabilities of Sb/CNT composite film anodes[76]. (C) Schematic illustration and rate capabilities of a nanorod-in-nanotube-structured Sb/N-C anode[77]. This figure is reproduced with permission from Liu *et al.*[75], Schulze *et al.*[76], and Luo *et al.*[77]

carbon coating improved electronic conductivity and facilitated Li-ion diffusion. Consequently, the nanorod-in-nanotube Sb/N-C anode delivered an impressive rate capability of 343 mAh g^{-1} after 45 cycles at a rapid current rate of 20 A g^{-1}. The porous structure provided additional space to accommodate volume changes during discharging and charging, whereas the robust multidimensional structure maintains both mechanical and electrical connections to improve cycling stability.

To achieve high-performance Sb-based anodes for LIBs, various strategies involving Sb-based alloys and carbon composites have been proposed for use as high-performance Sb-based anodes in LIBs[78-88]. Zhang *et al.* developed an Sb/C nanosheet anode to improve cycling and rate performance [Figure 8A][78]. Encapsulating Sb nanoparticles within carbon nanosheets effectively mitigated volume expansion and particle agglomeration during cycling while simultaneously minimizing direct electrolyte exposure. The Sb/C nanosheet anode demonstrated a highly reversible capacity of 598 mAh g^{-1} after 100 cycles at a current rate of 200 mA g^{-1}. Pan *et al.* synthesized NiSb/N-C nanosheets that delivered outstanding rates and long-life cycling performance [Figure 8B][79]. The NiSb alloy nanoparticles inserted into a matrix of N-doped carbon nanosheets provided structural stability by inhibiting direct contact between the alloy nanoparticles and the electrolyte and preventing alloy nanoparticle agglomeration during cycling. The NiSb/N-C nanosheets exhibited improved cycling and rate performance, delivering a stable capacity of 401 mAh g^{-1}

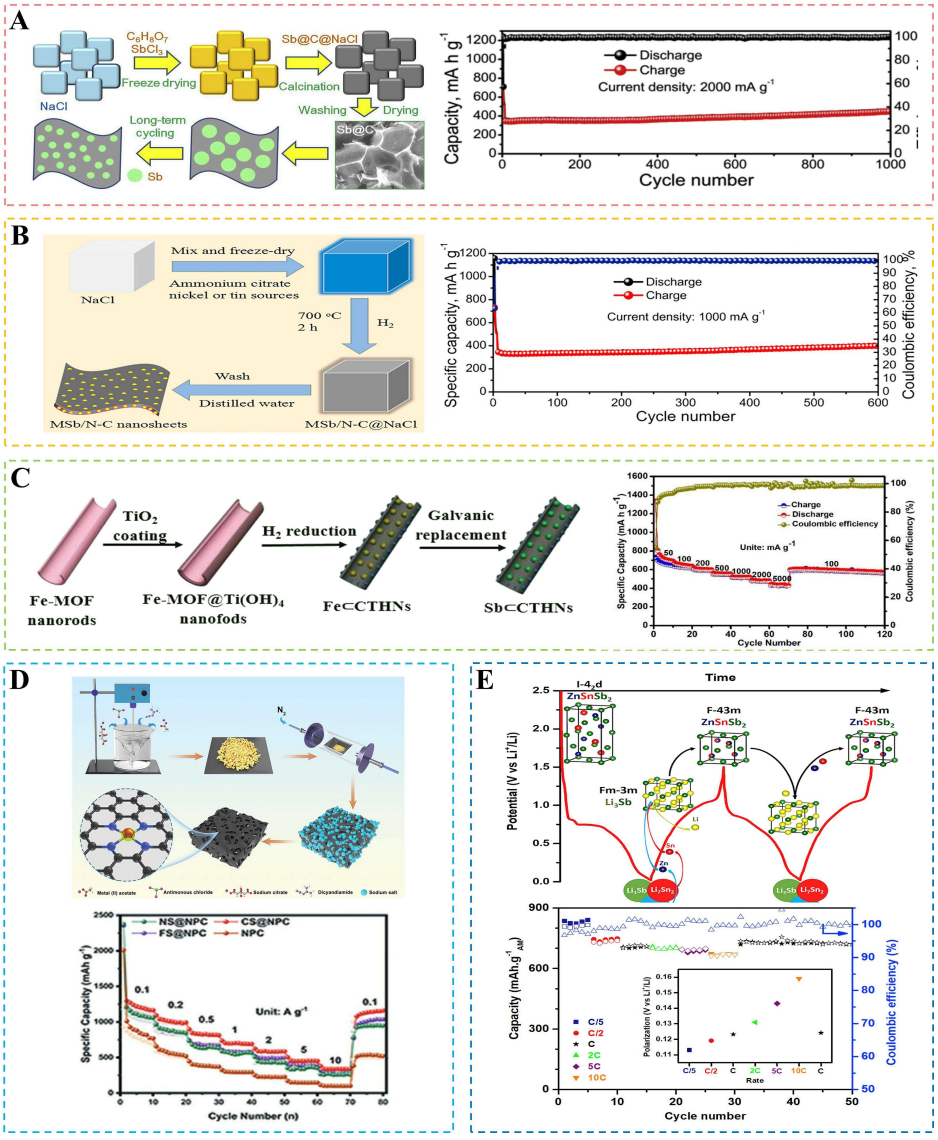

Figure 8. (A) Schematic illustration and cyclability of an Sb/C nanosheet anode[78]. (B) Schematic illustration and cyclability of a NiSb/N-C nanosheet anode[79]. (C) Schematic illustration and rate capability of an Sb/CTHN anode[80]. (D) Schematic illustration and rate capability of a CS/NPC anode[81]. (E) Schematic illustration and rate capability of a $ZnSnSb_2$ anode[82]. This figure is reproduced with permission from Zhang *et al.*[78], Pan *et al.*[79], Yu *et al.*[80], Yang *et al.*[81], and Coquil *et al.*[82].

after 1,000 cycles at a current rate of 1.0 A g^{-1}. Yu *et al.* encapsulated Sb nanoparticles derived from MOFs in hollow carbon and titanium dioxide nanotubes (Sb/CTHNs) to suppress volume expansion and enhance Li^+ diffusion [Figure 8C][80]. The Sb/CTHNs provide a large surface area and pathways for Li-ion diffusion and electron transport. The robust hollow structure accommodated volume expansion during the alloying/dealloying process, resulting in a stable SEI layer and a high rate capability of 374.1 mAh g^{-1} at a current rate of 5.0 A g^{-1}. Yang *et al.* fabricated a CoSb nanocomposite anchored on Swiss-cheese-like nitrogen-doped porous carbon (CS/NPC), which delivered stability and a high rate capability [Figure 8D][81]. The specific structure contributed to enhanced electronic conductivity, a shorter ion-diffusion distance, and suppressed Sb volume changes during repeated cycling. The CS/NPC anode exhibited a high rate capability of 343 mAh g^{-1} at a current rate of 10 A g^{-1}. The strong metal-N-C bonds formed by the doped heteroatoms provided sufficient active sites for Li ions and strengthened interfacial adhesion between the active materials

and the current collector. Coquil *et al.* reported ternary $ZnSnSb_2$ as a new LIB anode material [Figure 8E][82]. The $ZnSnSb_2$ anode exhibited a reversible capacity of 615 mAh g^{-1} with a capacity retention of 84.2% after 200 cycles when evaluated galvanostatically at a current rate of 252 mA g^{-1}; this high electrochemical performance is attributable to the distinctive quasi-topotactic reaction mechanism associated with $ZnSnSb_2$ during lithiation/delithiation. Su *et al.* synthesized a NiSb alloy embedded in N-doped carbon (NiSb/C) to enhance the electrochemical performance of Sb-based anodes for LIBs[83]. The NiSb/C anode exhibited good cycling stability and high rate performance, with the elemental Ni suppressing volume expansion and the N-doped carbon serving as a conductive network with sufficient active sites. Consequently, the NiSb/C anode demonstrated a reversible capacity of 426 mAh g^{-1} after 450 cycles at a current rate of 2 A g^{-1}. In short, carbon-based composite materials effectively suppress volume expansion and improve electron/ion diffusion characteristics, resulting in enhanced cycling stability and rate capabilities. Alloy materials have also been reported to exhibit less volume expansion during charging and discharging owing to their unique insertion or conversion reaction mechanisms. Regarding the electrolyte, the FEC additive was found to be essential. An unprecedented LiFSI salt was applied to an Sb anode, and its performance was evaluated. Recent LIB studies have transcended simple approaches. Instead of focusing on a single breakthrough, researchers have reported significant performance enhancements by combining multiple effective improvements. This trend highlights the need to engineer complex and advanced anode materials for next-generation LIBs. Regarding the electrolyte, the FEC additive was found to be essential, and a promising LiFSI salt was evaluated with the Sb-based anode. Table 2 summarizes recent advancements in Sb-based LIB anodes.

Sb-based SIB anodes

Sb has been extensively researched as a high energy density SIB anode material due to its high Na-storage capacity (Na_3Sb: 660 mAh g^{-1}) and appropriate operating voltage (0.3-0.7 V *vs.* Na^+/Na). However, Sb anodes exhibit drawbacks similar to those of LIBs, including the formation of unstable SEI layers, significant volume changes (~291%), and sluggish charge transfer during discharging and charging, resulting in poor cycling stability. To address these issues, recent advances in SEI layer control, structural control, and composite/alloy formation have been proposed for Sb-based anodes for SIBs.

Electrolyte additives significantly affect the formation of a stable SEI layer, which is closely related to the electrochemical performance of the Sb anode[72,89,90]. Lu *et al.* investigated the surface structure, composition, and electrochemical performance of Sb-based anodes (SiC-Sb-C) in FEC-free and FEC-containing electrolytes using XPS, Fourier transform infrared spectroscopy (FTIR), EIS, and electrochemical characterization techniques [Figure 9A][89]. Carbonate solvents (EC and DEC) gradually decompose on the SiC-Sb-C particle surface in the FEC-free electrolyte to form an SEI layer composed of Na_2CO_3, $ROCO_2Na$, and RONa units. The precipitate layers formed from these salts are generally loose, forming thick SEI layers. FEC-containing electrolyte is more reactive than EC or DEC-containing electrolyte; it decomposes first on the particle surface to form a dense and thin SEI layer composed of fluorine (F)-containing salts, such as NaF, F-$ROCO_2Na$, and F-RONa. Although a F-containing SEI film can inhibit the decomposition of EC and DEC to a certain extent, EC and DEC still decompose along with FEC at low potentials (below 0.5 V *vs.* Na^+/Na), resulting in the formation of a double-layer SEI film. The formation of a dense and thin double-layer SEI film improves the electrochemical performance of the Sb anode. Bian *et al.* investigated the effect of the FEC additive on the Sb anode for SIBs [Figure 9B][72]. The optimal concentration of FEC (10 vol%) provides a stable and NaF-rich SEI layer that alleviates Sb volume changes and inhibits continuous electrolyte decomposition. Consequently, the microsized Sb anode with an FEC-containing electrolyte exhibited a reversible capacity of 540 mAh g^{-1} with a retention of 85.3% after 150 cycles at 200 mA g^{-1}. Bodenes *et al.* revealed the role that binders play in determining the thickness, homogeneity, and chemical composition of the SEI layer formed on the surface of the Sb anode in a SIB

Table 2. Li-storage properties of Sb-based LIB anodes

Material	Electrolyte		Binder	ICE (%)	Cyclability after the Xth cycle (mAh g^{-1})	Rate capability		Ref.
	Salt	Solvent				Current rate (A g^{-1})	Reversible capacity (mAh g^{-1})	
Micro-sized Sb	1.0 M $LiPF_6$	PC with 10 vol% FEC	CMC	81.0	540 (X = 150)	5.0	575	[72]
Bulk Sb	1.2 M LiFSI	TEP:HFE = 1:3 mol%	PAA/CMC	87.5	648 (X = 50)	0.5	604	[73]
Pristine Sb	3.0 M LiFSI + 0.4 M $LiNO_3$	DOL:DME = 1:1 vol%	PAA/CMC	82.5	624 (X = 100)	3.3	487	[74]
Spherical Sb/C	1.0 M $LiPF_6$	EC:DMC = 1:1 vol% with 5 vol% FEC	Alginate	86.7	590 (X = 80)	1.2	535	[75]
Sb/CNT composite film	1.0 M $LiPF_6$	EC:DEC = 3:7 vol%	Binder-free	78.7	340 (X = 100)	3.2	300	[76]
Nanorod-in-nanotube Sb/N-C	1.0 M $LiPF_6$	EC:DMC:EMC = 1:1:1 vol% with 10 wt% FEC	CMC	78.3	346 (X = 3,000)	20.0	343	[77]
Sb/carbon nanosheets	1.0 M $LiPF_6$	EC:DMC = 1:1 vol%	PVDF	62.5	598 (X = 100)	2.0	449	[78]
NiSb/N-C nanosheets	1.0 M $LiPF_6$	EC:DMC = 1:1 vol%	PTFE	71.8	401 (X = 1,000)	5.0	252	[79]
Sb/CTHNs	1.0 M $LiPF_6$	EC:DEC = 1:1 vol% with 5 vol% FEC	PVDF	52.4	607 (X = 100)	5.0	435	[80]
CS/NPC	1.0 M $LiPF_6$	EC:DEC:DMC = 1:1:1 vol%	CMC	52	833 (X = 3,000)	10.0	343	[81]
$ZnSnSb_2$	1.0 M $LiPF_6$	PC:EC:DMC = 1:1:3 vol% with 5 vol% FEC + 1 vol% VC	CMC	83.0	615 (X = 200)	0.63	650	[82]
NiSb/C	1.0 M $LiPF_6$	EC:DEC = 1:1 vol% with 5 vol% FEC	Alginate	68.5	500 (X = 200)	2.0	426	[83]
NiSb/C nanosheets	1.0 M $LiPF_6$	EC:DEC = 1:1 vol%	PVDF	64.1	405 (X = 1,000)	2.0	305	[84]
Sb/rGO	1.0 M $LiPF_6$	EC:DMC = 1:1 vol%	PVDF	52.3	798 (X = 200)	0.43	563	[85]
silica-reinforce Sb/CNF	1.0 M $LiPF_6$	EC:DMC = 1:1 vol%	PAA	66.4	700 (X = 400)	1.0	468	[86]

system using XPS and electrochemical testing[90]. Sb was detected in the Sb 3d XPS spectrum of the Sb-carboxymethyl cellulose (CMC) anode in the fully desodiated state, consistent with the partial redissolution of the SEI layer (dissolution of Na_2O/NaOH). In contrast, Sb was not detected on the Sb-PVDF anode in the fully desodiated state because the SEI layer covering the Sb anode was more than 5 nm thick. Therefore, a more uniform and thinner SEI layer was formed in the case of the Sb-CMC anode compared to the Sb-PVDF anode, resulting in superior electrochemical performance [Figure 9C].

Nanostructural design and low-dimensional engineering aimed at accelerating reaction kinetics are considered the most efficient strategies for addressing the abovementioned drawbacks, including the sluggish rate capability and rapid capacity decay associated with the excessive volume change experienced by Sb[67,91-96]. Liu *et al.* fabricated highly uniform Sb nanotubes (NTs) using a galvanic replacement approach using a Cu_2Sb-mediated formation mechanism[91]. The Sb NT anode delivered a reversible capacity of 546 mAh g^{-1} after 100 cycles with a capacity retention of 98.7% at 0.1 A g^{-1} and excellent long-term cycling stability at 1.0 A g^{-1} (342 mAh g^{-1} after 6,000 cycles with a capacity retention of 74%) [Figure 10A]. The excellent Na-storage performance of the Sb NTs was attributed to the one-dimensional hollow structure, which effectively relieves structural deformation and shortens the ion-diffusion path, thereby improving

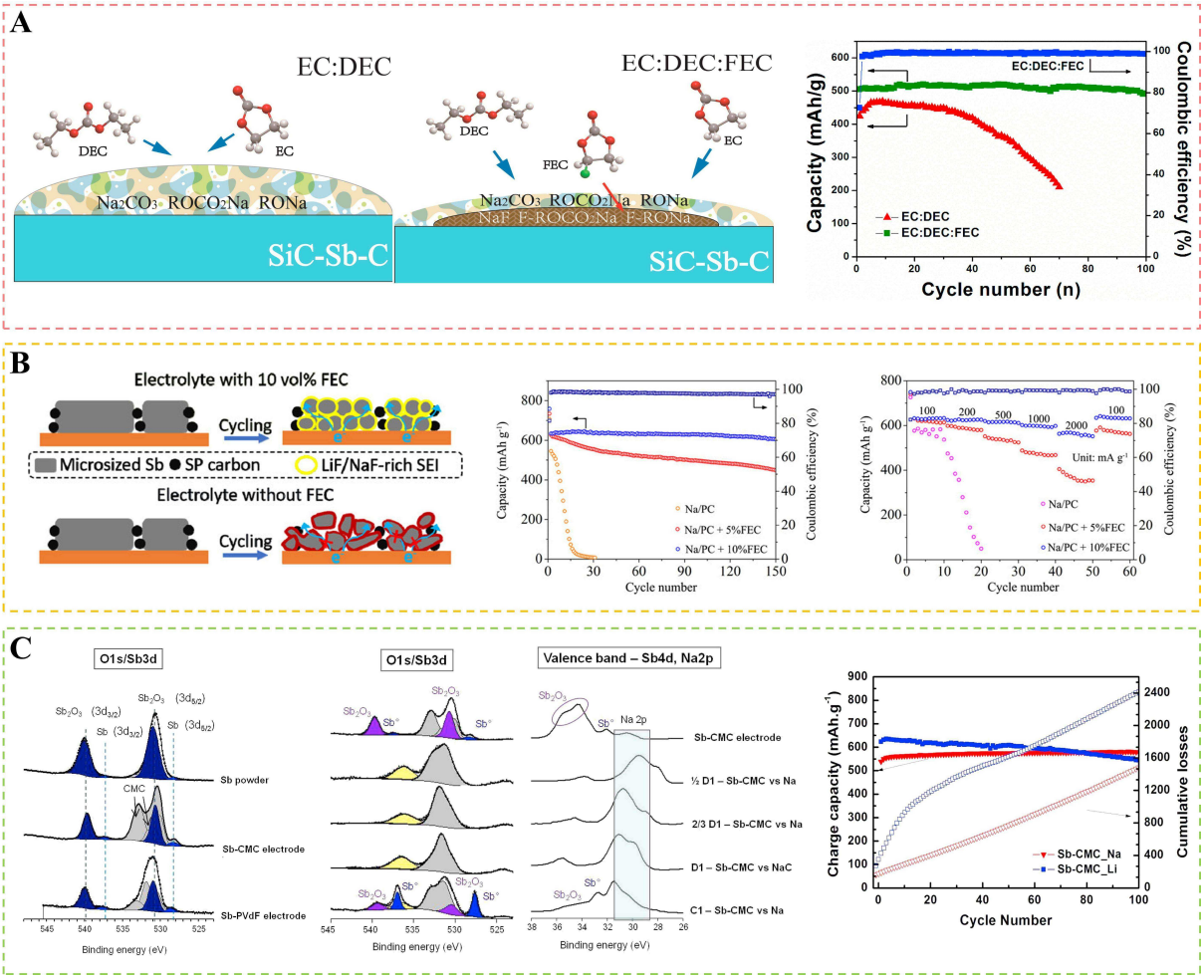

Figure 9. (A) Schematic illustration of the SEI layer formation mechanism and the cyclabilities of Sb-based anodes in FEC-free and FEC-containing electrolytes[89]. (B) Schematic illustration, cyclabilities, and rate capabilities associated with morphological changes experienced by micro-sized Sb anodes in FEC-free and 10 vol% FEC-containing electrolytes[72]. (C) XPS results and cyclabilities of Sb-CMC anodes[90]. This figure is reproduced with permission from Bian *et al.*[72], Lu *et al.*[89], and Bodenes *et al.*[90].

the Na-ion diffusion kinetics. Tian *et al.* synthesized two-dimensional few-layer antimonene (2D FLA) nanosheets *via* liquid-phase exfoliation of β-antimony in a 1:1 mixture of *N*-methyl pyrrolidone (NMP) and ethanol[67]. The 2D FLA anode maintained a stable capacity of 620 mAh g^{-1} after 150 cycles at 0.5 C (330 mA g^{-1}) along with a capacity retention of 99.7% from cycles 10 to 150 [Figure 10B]. Fast Na-ion diffusion in 2D FLA was attributed to the small diffusion barrier of 0.14 eV, and its ability to efficiently accommodate anisotropic volume expansion along the a/b plane during cycling, thereby achieving high structural stability. Liu *et al.* synthesized a yolk-shell Sb/graphdiyne (GDY) nanobox with an inner void space as an anode material using a galvanic replacement reaction [Figure 10C][92]. The voids accommodate Sb volume changes, and the GDY shell, with its intrinsic in-plane cavities, facilitates Na-ion diffusion. This anode delivered a capacity of 593 mAh g^{-1} at 100 mA g^{-1}, with little loss of capacity observed after 200 cycles. The Sb/GDY nanobox anode was subjected to full-cell testing with $Na_3V_2(PO_4)_3$. The full cell delivered a capacity retention of 75% and a capacity of 354 mAh g^{-1}_{anode} after 500 cycles at 1 A g^{-1}_{anode}. The stable cycling performance of the spherical Sb/C anode is a result of its finely organized nanostructure that effectively accommodates volume changes and inhibits Sb-nanoparticle agglomeration. Li *et al.* designed a 3D porous carbon matrix containing Sb nanoparticles (Sb/3DPC) through polymer blowing and the use of a galvanic

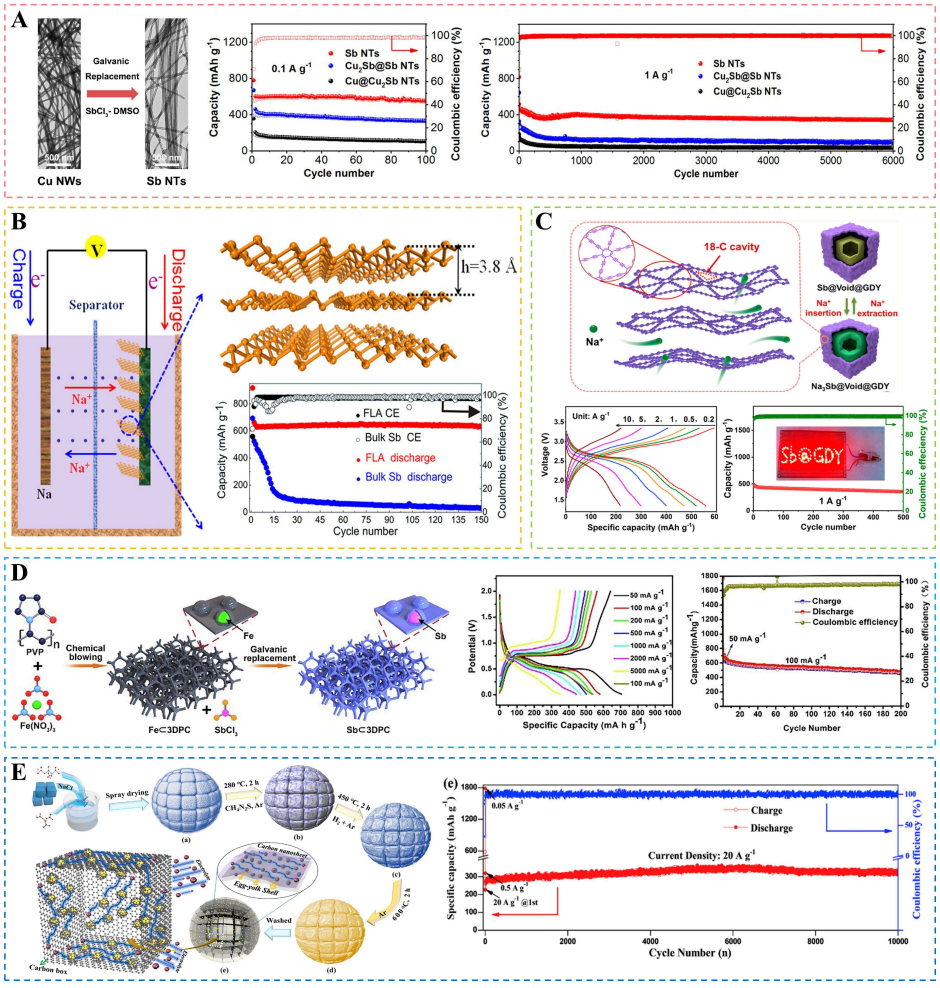

Figure 10. (A) TEM images of Cu nanowires as sacrificial templates and the performance of Sb NTs synthesized by galvanic replacement[91]. (B) Schematic illustration and atomic structure of 2D few-layer antimonene, and the cyclability of a 2D few-layer antimonene anode[67]. (C) Schematic illustration, cyclabilities, and rate capabilities of a full cell with a yolk-shell Sb/graphdiyne nanobox anode[92]. (D) Schematic illustration of the fabrication of a 3D porous Sb/C anode and its rate capabilities[93]. (E) Schematic illustration and cyclability of a yolk-shell Sb/NS-3DPCMSs anode[94]. This figure is reproduced with permission from Tian *et al.*[67], Liu *et al.*[91], Liu *et al.*[92], Li *et al.*[93], and Chen *et al.*[94].

replacement method[93]; this architecture provided an enlarged electrode/electrolyte interface owing to its large pore volume and surface area, which shortened the Na-ion transfer path and inhibited volume expansion. The Sb/3DPC anode showed superior cycling stability, namely, 461 mAh g^{-1} over 200 cycles at 100 mA g^{-1} with a capacity retention of ~66% and an excellent rate capability of 346 mAh g^{-1} at 5 A g^{-1} [Figure 10D]. Chen *et al.* prepared yolk-shell-structured Sb@C using a continuous one-pot multistep strategy, with the Sb nanoparticles confined to the N and S co-doped 3D porous carbon microspheres (Sb/NS-3DPCMSs)[94]. Remarkably, the Sb/NS-3DPCMS anode exhibited a specific capacity of 331 mAh g^{-1} after 10,000 cycles at 20 A g^{-1} with almost 100% capacity retention [Figure 10E]. The robust yolk-shell structure provided sufficient space to effectively relieve the volume expansion experienced by Sb and stabilized the 3D architecture during long-term cycling. Furthermore, empty carbon boxes with rich hierarchical pores and high conductivities exhibited excellent rate performance by promoting fast Na-ion/electron transfer. Li *et al.* synthesized various multidimensional Sb nanostructures as SIB anode materials using a chemical dealloying approach[95]. The 0D Sb nanoparticles (Sb-NPs), 2D Sb nanosheets (Sb-NSs), and 3D nanoporous (NP) Sb were synthesized by modifying the dealloying reaction kinetics using different

etching solvents. Among the various nanostructures, the Sb-NS anode showed a high reversible capacity of 620 mAh g^{-1} after 100 cycles, with a capacity retention of 90.2% at 100 mA g^{-1}. Furthermore, the Sb-NS anode delivered high rate capabilities at various current densities in the 100-6,400 mA g^{-1} range. The excellent electrochemical performance of the 2D nanostructure is ascribable to its high Na-ion availability, robust structural unity, and fast reaction kinetics. Yang *et al.* also fabricated 0D Sb nanoparticles, 2D antimonene nanosheets, and 3D porous Sb networks by electrochemically delaminating bulk Sb and exploiting varying reaction mechanisms in distinct electrolytes[96]. The 2D antimonene nanosheet anode delivered a high reversible capacity of 572.5 mAh g^{-1} after 200 cycles at 0.2 A g^{-1} (capacity retention: 91.5%) and a superior rate capability of 553.6 mAh g^{-1} at 5 A g^{-1}. Among these multidimensional strategies, the use of 2D shapes is particularly well-suited for accommodating the volume expansion experienced by Sb anodes in SIBs.

Sb-based alloys and carbon composites have also been proposed in the SIB system to achieve high performance by effectively mitigating the significant volume changes experienced by Sb during sodiation/desodiation[97-104]. Ma *et al.* synthesized an ultrafine mesoporous Sb_2O_3@Sb nanocomposite using a one-step dealloying reaction and a two-phase Mg-Sb precursor[97]. The mesoporous Sb_2O_3@Sb anode exhibited a high specific capacity of 659 mAh g^{-1} in the second cycle, long-term cycling stability (a capacity retention of 99.8% after 200 cycles at 0.2 A g^{-1}), and an excellent rate capability (200 mAh g^{-1} at 29.7 A g^{-1}) [Figure 11A]. Xie *et al.* developed an Sb@NGA-CMP composite comprising ultrafine Sb nanoparticles uniformly anchored in the pores of a covalent organic framework (COF) using an *in-situ* synthetic strategy[98]. To facilitate COF formation, Sb^{3+} was introduced as a catalyst and subsequently immobilized in the COF channels through reduction. This unique architecture provided electronic interactions between Sb nanoparticles and π-conjugated microporous polymers (CMPs) through nitrogen groups, thereby accelerating charge transfer along the COF. The Sb@NGA-CMP composite anode exhibited a high rate capability of 223 mAh g^{-1} at 2 A g^{-1}, and 188 mAh g^{-1} at 5 A g^{-1}, and excellent Na storage performance of 320 mAh g^{-1} after 160 cycles at 0.2 A g^{-1} [Figure 11B]. Zheng *et al.* developed a cauliflower-shaped Sb/NiSb composite by an electrodeposition process[99]. The cauliflower-like structure enhanced electron transfer and shortened the Na-ion transport length, while the inactive Ni contributed to high conductivity and suppressed significant volume changes during cycling. These factors collectively contributed to stable cycling performance (521 mAh g^{-1} after 100 cycles with a capacity retention of 96% at 100 mA g^{-1}) and a high rate capability (above 400 mAh g^{-1} at 2,000 mA g^{-1}) [Figure 11C]. Ma *et al.* synthesized a bimetallic single-phase NP SnSb alloy by dealloying a ternary Mg-Sn-Sb precursor[100]. The NP-SnSb-alloy anode delivered a specific capacity of 506.6 mAh g^{-1} after 100 cycles with a capacity retention of 94.5% at 0.2 A g^{-1} and 457.9 mAh g^{-1} after 150 cycles at 1.0 A g^{-1} (capacity retention: 95.5%); in addition, it exhibited a superior rate capability with a specific capacity of 458.5 mAh g^{-1} at 10 A g^{-1} [Figure 11D]. Gao *et al.* fabricated nanoporous (np) Bi-Sb alloys (Bi_2Sb_6, Bi_4Sb_4, and Bi_6Sb_2) by one-step dealloying ternary Mg-based precursors[101]. The np-Bi_2Sb_6-alloy anode showed the best cycling stability, exhibiting a specific capacity of 257.5 mAh g^{-1} after 2,000 cycles at 200 mA g^{-1}, which corresponds to a capacity loss of 0.027% per cycle. Notably, the np-Bi_2Sb_6 anode exhibited remarkable long-term cycling performance, even at 1 A g^{-1}, maintaining a specific capacity of 150 mAh g^{-1} after 10,000 cycles with a capacity decay of 0.0072% per cycle [Figure 11E]. The outstanding electrochemical performance of np-Bi_2Sb_6 is attributable to its NP structure with an optimal Bi/Sb atomic ratio; this structure not only alleviated the volume expansion of the active material but also effectively promoted electrolyte permeation and the transfer of electrons and ions. Pan *et al.* prepared watermelon-like nanostructures composed of Sb nanocrystals dispersed in amorphous $TiPO_x$ (c-Sb@a-TiO_x) by hydrolyzing tetrabutyl titanate in the presence of $SbPO_4$ nanorods, followed by calcination[102]. The c-Sb@a-TiO_x anode delivered a specific capacity of 147 mAh g^{-1} after 1,000 cycles at 1.0 A g^{-1} with a capacity retention of 82%. In a similar manner to that observed for LIBs, composite materials with carbon effectively suppress volume expansion, improve electron/ion diffusion, and enhance cycling stability and rate capability. Alloy materials,

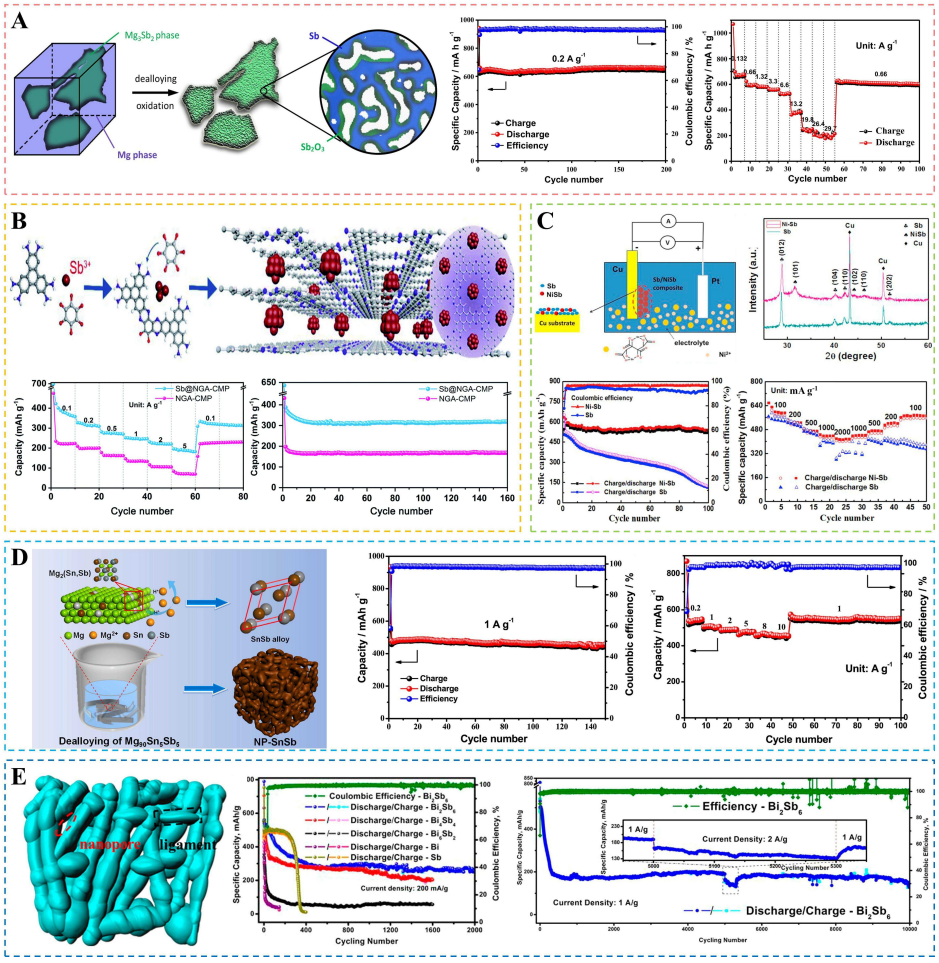

Figure 11. (A) Schematic illustration of the fabrication process, cyclability, and rate capability of a mesoporous Sb_2O_3@Sb nanocomposite anode[97]. (B) Schematic illustration of the fabrication process and rate capability of an Sb@NGA-CMP composite anode[98]. (C) Schematic illustration, XRD patterns, cyclability, and rate capability of an electrodeposited Sb/NiSb composite anode[99]. (D) Schematic illustration of the one-step dealloying process used to prepare the NP-SnSb alloy anode, along with its cyclability and rate capability[100]. (E) Structure and cyclability of a ligament-channel np-Bi-Sb alloys anode[101]. This figure is reproduced with permission from Ma *et al.*[97], Xie *et al.*[98], Zheng *et al.*[99], Ma *et al.*[100], and Gao *et al.*[101].

with their unique reaction mechanisms (insertion or conversion reactions), also exhibit less volume expansion during charging and discharging. Various approaches that are similar to those used for LIBs have been reported for alleviating the significant volume changes experienced by Sb anodes in SIBs. Recent research revealed that structural engineering and composite/alloy approaches are also effective for SIBs. Additionally, an optimal combination of electrolyte composition and additives, including FEC, was determined to facilitate the formation of a stable SEI layer. Recent advances in Sb-based anodes for SIBs are summarized in Table 3.

Sb-based PIB anodes

Sb is accomplished prospective candidate as high-capacity PIB anodes owing to its high theoretical gravimetric and volumetric capacities (660 mAh g^{-1} and 4,420 mAh cm^{-3}) compared to those of graphite (279 mAh g^{-1} and 631 mAh cm^{-3}), Si (954 mAh g^{-1} and 2,223 mAh cm^{-3}), and Sn (226 mAh g^{-1} and 1,652 mAh cm^{-3}), as summarized in Table 1. However, Sb experiences substantial volume changes of up to 405.7% (K_3Sb) in a PIB, which is higher than those of graphite (63.1%, KC_8), Si (216.7%, KSi), and Sn

Table 3. Na-storage properties of Sb-based anodes for SIBs

Material	Electrolyte		Binder	ICE (%)	Cyclability after the Xth cycle (mAh g^{-1})	Rate capability		Ref.
	Salt	Solvent				Current rate (A g^{-1})	Reversible capacity (mAh g^{-1})	
Sb nanotubes	1.0 M $NaClO_4$	EC:DMC = 1:1 vol% with 5 vol% FEC	CMC	71.0	342 (X = 6,000)	0.1	546	[91]
Few-layer antimonene	1.0 M $NaClO_4$	EC:DEC = 1:1 vol% with 5 vol% FEC	CMC	64.7	620 (X = 150)	0.33	400	[67]
Spherical Sb/C	1.0 M $NaClO_4$	EC:PC = 1:1 vol% with 5 vol% FEC	Alginate	66.9	502 (X = 150)	1.2	340	[75]
Sb/graphdiyne nanobox	1.0 M $NaClO_4$	EC:DMC = 1:1 vol% with 5 vol% FEC	CMC	45.6	325 (X = 8,000)	10.0	294	[92]
3D porous Sb/C	1.0 M $NaClO_4$	PC with 5 wt% FEC	PVDF	38.0	461 (X = 200)	5.0	349	[93]
Yolk-shell Sb/NS-3DPCMSs	1.0 M $NaClO_4$	PC with 5 wt% FEC	CMC	48.1	540 (X = 150)	20	331	[94]
Sb nanosheets	1.0 M $NaPF_6$	EC:DEC = 1:1 vol% with 5 vol% FEC	PAA/CMC	62.4	559 (X = 100)	5.0	359	[95]
2D antimonene nanosheet	1.0 M $NaPF_6$	EC:DMC = 1:1 vol% with 5 vol% FEC	CMC	77.0	642 (X = 200)	5.0	554	[96]
Sb_2O_3/Sb	1.0 M $NaClO_4$	PC with 5 vol% FEC	CMC	67.9	659 (X = 200)	0.3	200	[97]
Sb/COF	1.0 M $NaClO_4$	EC:DMC = 1:1 vol% with 5 vol% FEC	Alginate	58.5	320 (X = 160)	1.0	344	[98]
Sb/NiSb	1.0 M $NaClO_4$	EC:PC = 1:1 vol% with 5 vol% FEC	Binder-free	86.0	521 (X = 100)	2.0	400	[99]
Nanoporous SnSb	1.0 M $NaClO_4$	PC with 5 wt% FEC	PVDF	58.0	507 (X = 100)	1.0	458	[100]
Bi_2Sb_6	1.0 M $NaClO_4$	PC with 5 wt% FEC	CMC	69.8	258 (X = 2,000)	1.0	150	[101]
Sb/$TiPO_x$	1.0 M $NaClO_4$	PC with 3 wt% FEC	Alginate	42.3	286 (X = 100)	1.0	147	[102]

(180.8%, KSn). Therefore, alleviating these volume changes is crucial for realizing high-capacity Sb-based anodes. In this section, we briefly summarize recent studies related to various strategies aimed at achieving high-capacity Sb anodes for PIBs, including SEI layer control, structural control, and composite/alloy formation.

To confirm the effects of forming an artificial SEI layer, we introduce several relevant studies based on their high electrochemical performance[105-107]. Zhang *et al.* reported effective electrolytes, including potassium hexafluorophosphate (KPF_6) and potassium bis(fluorosulfonyl)imide (KFSI) salts, using Sb-, Bi-, and Sn-based PIB anodes [Figure 12A][105]. Generally, the KPF_6 electrolyte contributes to the formation of an unstable SEI layer, which is incapable of protecting against electrolyte decomposition during repeated cycling. In contrast, the KFSI electrolyte provides a stable SEI layer with superior mechanical and electrical properties on the surface of the active material; this stable SEI layer effectively protects against electrolyte decomposition by reducing side reactions and providing smooth K-ion pathways, which is ascribable to the layers formed on the surfaces of the active materials. Based on the effect of the KFSI electrolyte, the Sb/C anode exhibited stable cycling performance with a reversible capacity of 470 mAh g^{-1} using 1 M KFSI in EC/DEC as the electrolyte after 50 cycles. Zhou *et al.* reported an optimal K-ion electrolyte for high-performance Sb in PIB systems, which was obtained by tuning the electrolyte composition

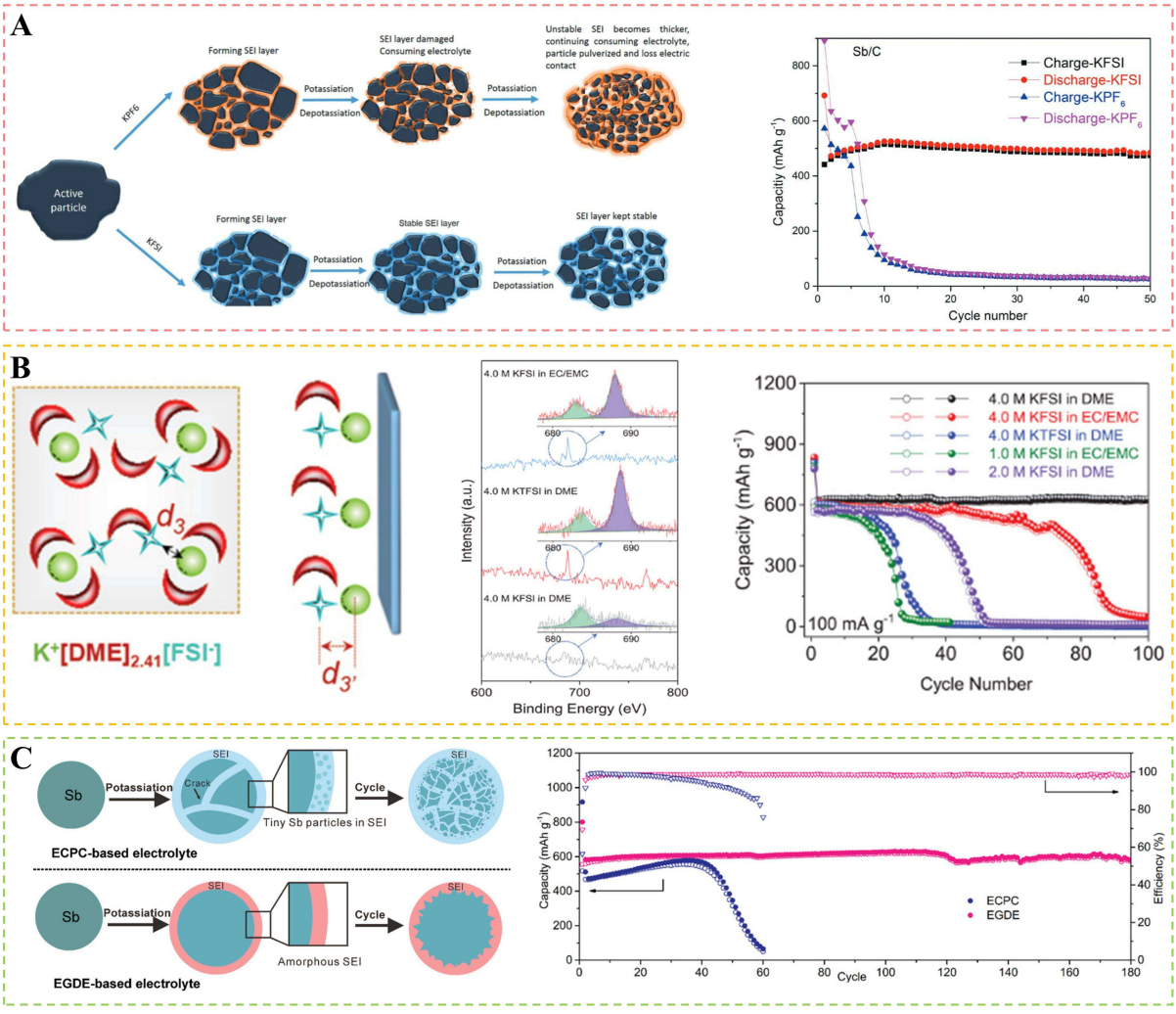

Figure 12. (A) Schematic illustration and cyclabilities of an Sb/C anode using KPF_6- and KFSI-salt-based electrolytes[105]. (B) Schematic illustration and cyclabilities of a pristine Sb anode using carbonate and ether-based electrolytes[106]. (C) Schematic illustration and cyclability of a commercial Sb anode using an EGDE-based electrolyte[107]. This figure is reproduced with permission from Zhang *et al.*[105], Zhou *et al.*[106], and Du *et al.*[107].

(i.e., anion, solvent, and concentration) [Figure 12B][106]. The proposed electrolyte (4 M KFSI in DME) contributed to the excellent cycling performance of the Sb anode, with an extremely high reversible capacity of 628 mAh g^{-1} obtained after 100 cycles at a current rate of 100 mA g^{-1}. This performance is ascribable to the powerful interaction between FSI^- and K^+ at the bulk Sb electrode surface in DME. Du *et al.* proposed an ether-based electrolyte to accommodate the volume change experienced by the Sb anode in a PIB during cycling [Figure 12C][107]. The KFSI electrolyte in ethylene glycol diethyl ether (EGDE) contributed to the outstanding cycling performance owing to its enhanced maximum elastic strain. In addition, the EGDE electrolyte suppressed the pulverization of Sb particles and prevented the formation of an additional SEI layer. Consequently, the Sb anode exhibited a reversible capacity of ~573 mAh g^{-1} with a capacity retention of nearly 100% after 180 cycles at a current rate of 100 mA g^{-1} using the EGDE electrolyte. In short, an effective SEI layer was formed by the optimal combination of the KFSI salt and the DME and EGDE solvents, thereby contributing to the excellent cycling characteristics associated with the chemical and mechanical properties of the SEI layer.

Various approaches involving multidimensional structures have been reported for structural control of Sb-based anodes in PIBs[108-112]. Shi *et al.* developed a flower-like $Sb_4O_5Cl_2$ cluster, which was prepared by a hydrothermal method, for PIB use [Figure 13A][108]. The flower-like structure provides diffusion paths for K ions inserted in parallel along its plane. Furthermore, a flower-like $Sb_4O_5Cl_2$ anode exhibited high reversible capacities of 530, 316, and 150 mAh g^{-1} at rates of 50, 100, and 150 mA g^{-1}, respectively. Liu *et al.* suggested the use of honeycomb-like porous microsized layered Sb (porous-Sb) [Figure 13B][109]; the porous Sb was prepared using a template-free hydrothermal method with deionized water. The honeycomb-like porous structure not only provided efficient K-ion transport but also extra space for accommodating volume changes. Based on its structural benefits, porous-Sb exhibited good electrochemical cycling stability with an initial reversible capacity of 655.5 mAh g^{-1} and a capacity retention of 84% after 80 cycles at a current rate of 50 mA g^{-1}. Imtiaz *et al.* reported Sb deposited on a $Cu_{15}Si_4$ ($Sb/Cu_{15}Si_4$) nanowire array as an anode, which was synthesized by high-boiling-solvent-mediated vapor-solid-solid growth, with the aim of enhancing the electrochemical performance of Sb [Figure 13C][110]. The $Sb/Cu_{15}Si_4$ nanowire contributed to the outstanding electrochemical performance owing to its mechanically robust, highly stable, and distinctive structure. Furthermore, the $Sb/Cu_{15}Si_4$ nanowire anode exhibited a high initial reversible capacity of 647.9 mAh g^{-1} at a current rate of 50 mA g^{-1} and good cycling performance, with a capacity retention of 65% over 1,250 cycles at a high 200 mA g^{-1} rate. Guo *et al.* proposed an MXene-based aerogel containing single Sb atoms, quantum dots, and graphene oxide (Sb-SQ@MA) [Figure 13D][111], which was chemically synthesized using few-layered MXene ($Ti_3C_2T_x$), graphene oxide (GO), and $SbCl_3$ as precursors. The high electrochemical performance of Sb-SQ@MA was achieved through improved charge-transfer kinetics, enhanced K-storage capability, structural stability, and highly efficient electron transfer. The Sb-SQ@MA anode exhibited a stable capacity retention of 94% with a high reversible capacity of 314 mAh g^{-1} after 1,000 cycles at a fast current density of 1 A g^{-1}. Consequently, various structural controls have contributed to the stable high rate capability and cycling performance of Sb-based PIB anodes owing to their distinctive structural characteristics that accommodate volume expansion or facilitate K-ion diffusion. He *et al.* fabricated a 3D macroporous Sb@C composite (Sb@C-3DP) using a simple KCl template [Figure 13E][112]; Sb@C-3DP showed a reversible capacity of 516 mAh g^{-1} at 50 mA g^{-1}, an ICE of 76.2%, and delivered a capacity retention of 97% after 260 cycles at 500 mAh g^{-1}. A full cell with a Prussian blue cathode delivered a reversible capacity of 508 mAh g^{-1} (based on anode mass) at a current rate of 0.2 A g^{-1}.

Various strategies, such as alloy or composite formation, have been extensively studied for improving the electrochemical properties of Sb anodes for PIBs[12,69,70,105,110-119]. Zheng *et al.* designed Sb nanoparticles encapsulated in an interconnected carbon-sphere network (Sb/CSN) *via* an electrospray-assisted strategy [Figure 14A][69]. The uniformly dispersed nano-Sb within the porous spherical network mitigated the volume change experienced by Sb. In addition, the highly concentrated electrolyte formed a robust KF-rich SEI on the Sb/CSN surface. Synergy between this interesting structure and the robust SEI greatly enhanced the electrochemical performance of the Sb/CSN anode, which maintained a reversible capacity of 504 mAh g^{-1} after 220 cycles at 200 mA g^{-1}. Shi *et al.* encapsulated Sb nanoparticles in N-, S-, and F-co-doped carbon skeletons (Sb/NSF-C) using a hydrothermal method, heat treatment, and etching [Figure 14B][113]. Doping changes the electronic configuration, resulting in defects in the carbon layers. This 3D porous structure is highly mechanically strong and contributes to enhancing the electrochemical reaction kinetics. After 200 cycles, the Sb/NSF-C composite retained a reversible capacity of 287 mAh g^{-1} at a current rate of 1.0 A g^{-1}. Han *et al.* embedded Sb nanocrystals in an ultrathin carbon nanosheet (Sb/CNS) using a one-step solvothermal reaction [Figure 14C][114]. The mechanical stability of the nanosheet accommodated volume changes and suppressed side reactions involving the electrolytes. Moreover, the large surface area of the nanosheet contributed to fast ionic/electronic diffusion. Consequently, a reversible capacity of 247 mAh g^{-1} and up to 90% capacity retention were attained after 600 cycles at 200 mA g^{-1}. Cao *et al.* created a flexible integrated anode by confining Sb nanoparticles in porous carbon nanofibers

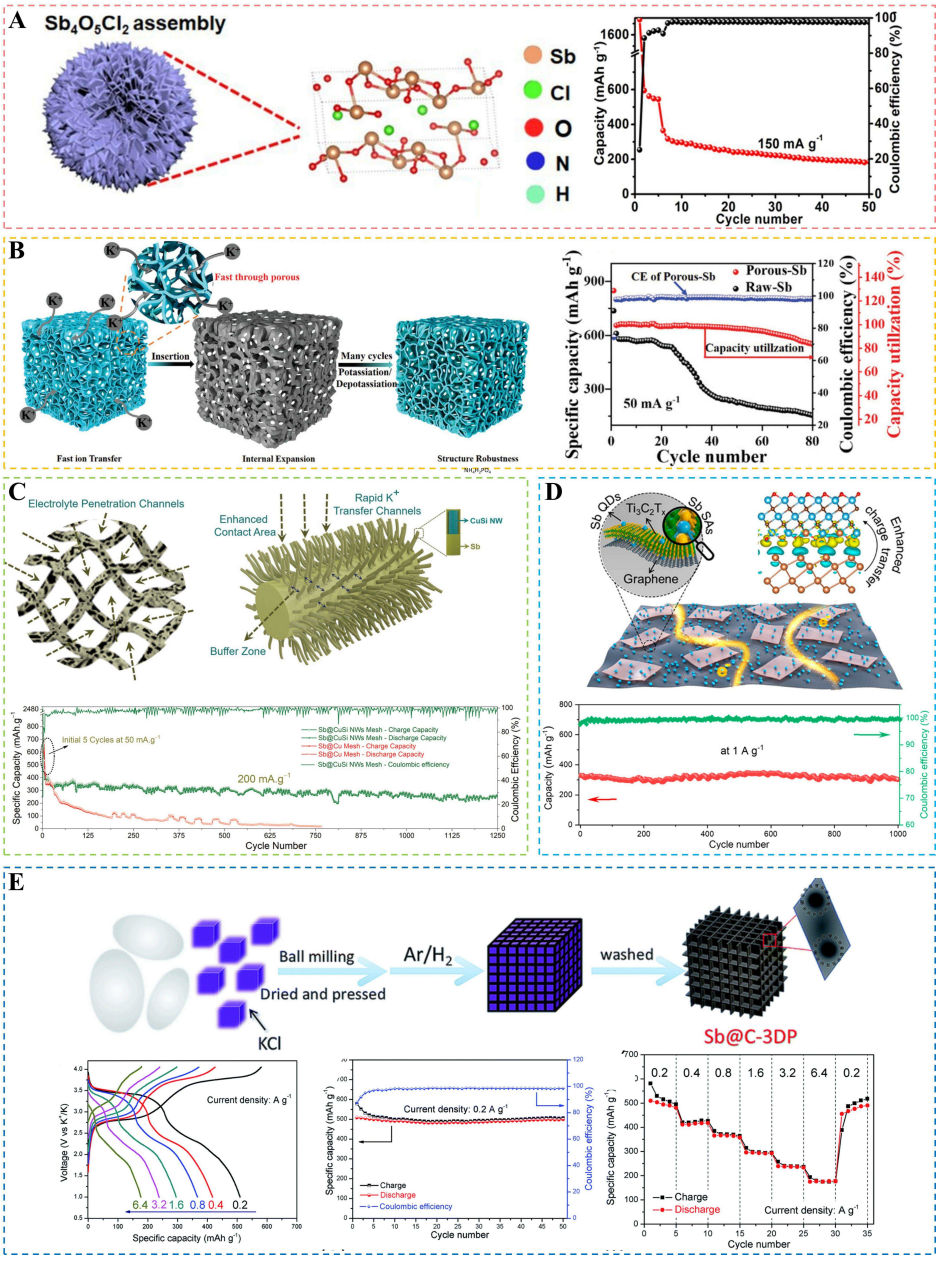

Figure 13. (A) Schematic illustration and cyclability of a flower-like $Sb_4O_5Cl_2$ PIB anode[108]. (B) Schematic illustration and cyclability of a honeycomb-like porous Sb anode for PIBs[109]. (C) Schematic illustration and cyclability of an Sb/$Cu_{15}Si_4$ nanowire anode for PIBs[110]. (D) Schematic illustration and cyclability of an Sb quantum dot/MXene-based aerogel PIB anode[111]. (E) Schematic illustration, cyclability, and rate capability of a full cell with a 3D macroporous Sb/C composite anode[102]. This figure is reproduced with permission from Shi *et al.*[108], Liu *et al.*[109], Imtiaz *et al.*[110], Guo *et al.*[111], and He *et al.*[112].

(Sb/C PNFs) using an electrospin-assisted strategy [Figure 14D][115]. The vessel-like channels in the 3D interconnecting carbon nanofibers promoted electrolyte flow and shortened the the K^+ diffusion way of the uniform Sb nanoparticles. The flexible porous carbon nanofibers function as a buffer matrix that mitigates volume expansion while simultaneously providing pathways for rapid electron transfer. As a result, a reversible capacity of 264.0 mAh g^{-1} was attained after 500 cycles at 2.0 A g^{-1}. Xiong *et al.* fabricated a BiSb/C composite nanosheet by embedding Bi-Sb alloy nanoparticles inside a porous carbon matrix via freeze-drying and pyrolysis [Figure 14E][116]. The BiSb alloy mitigated volume changes owing to the similar

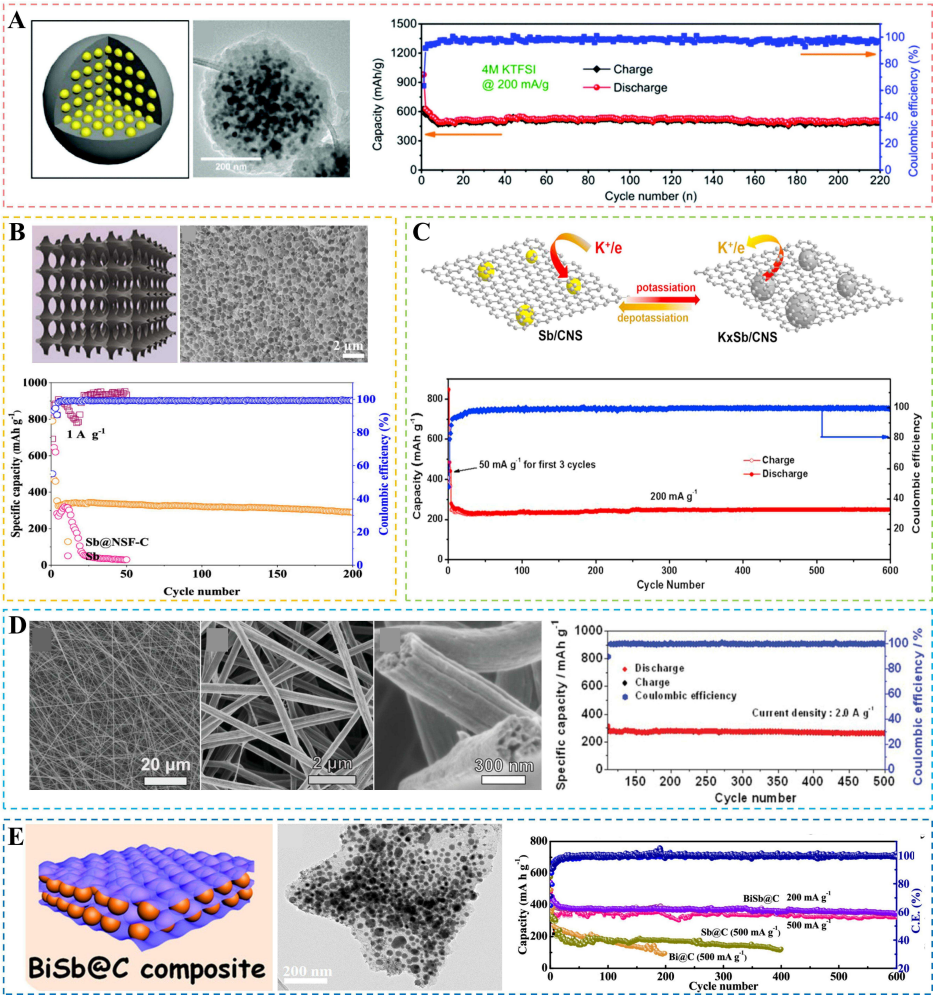

Figure 14. (A) Schematic illustration, SEM image, and cycling performance of an Sb/CSN PIB anode[69]. (B) Schematic illustration, SEM image, and cycling performance of an Sb/NSF-C PIB anode[113]. (C) Schematic illustration and rate performance of an Sb/CNS PIB anode[114]. (D) Schematic illustration, SEM images, and cycling performance of an Sb/C PNF PIB anode[115]. (E) Schematic illustration, SEM image, and cycling performance of a BiSb/C PIB anode[116]. This figure is reproduced with permission from Zheng *et al.*[69], Shi *et al.*[113], Han *et al.*[114], Cao *et al.*[115], and Xiong *et al.*[116].

physicochemical properties and infinite miscibility of Bi and Sb. Furthermore, the carbon effectively buffered the volume change of the BiSb alloy nanoparticles during cycling. The BiSb/C anode exhibited a reversible capacity of 320 mAh g^{-1} with a high capacity retention of 97.5% after 600 cycles at 500 mA g^{-1}. Diverse approaches have been explored to address the substantial volume changes experienced by Sb-based PIB anodes, including SEI layer control, structural control, and composite/alloy formation. Except for SEI layer control, these methods parallel the techniques used for LIBs and SIBs. While FEC additives are well-known for improving the performance LIBs and SIBs, their impact on PIBs remains controversial[120,121]. Using FEC as an additive for an anode in a half-cell system dramatically reduced the ICE while increasing the chemical and cycling stabilities of the system, demonstrating a trade-off relationship. Although a few studies have validated the potential of the FEC additive in various PIB systems, its application to Sb-based anodes remains unexplored. Therefore, the role of FEC in an Sb-based PIB anode requires further investigation. Recent progress in Sb-based PIB anodes is summarized in Table 4.

Table 4. K storage properties of Sb-based PIB anodes

Material	Electrolyte		Binder	ICE (%)	Cyclability after the Xth cycle (mAh g^{-1})	Rate capability		Ref.
	Salt	Solvent				Current rate (A g^{-1})	Reversible capacity (mAh g^{-1})	
Sb/C	1.0 M KFSI	EC:DEC = 1:1 vol%	CMC	64.6	470 (X = 50)	-	-	[105]
Pristine Sb	4.0 M KFSI	DME	PAA/CMC	74.2	628 (X = 100)	3.0	305	[106]
Commercial Sb	1.0 M KFSI	ethylene glycol diethyl ether	CMC	69.4	573 (X = 180)	0.5	443	[107]
Flower-like $Sb_4O_5C_{12}$	3.0 M KFSI	EC:DEC = 1:1 vol%	PVDF	27.8	190 (X = 40)	0.5	105	[108]
Honeycomb-like porous Sb	4.0 M KFSI	DME	PAA	74.4	551 (X = 80)	2.0	442	[109]
Sb/$Cu_{15}Si_4$ nanowire	4.0 M KFSI	DME	Binder-free	76.0	250 (X = 1,250)	4.0	105	[110]
Sb QD/ MXene aerogel	1.0 M KPF_6	EC:PC = 1:1 vol%	CMC	47.7	521 (X = 106)	3.2	246	[111]
3D macroporous Sb/C	5.0 M KFSI	DME	CMC	76.2	342 (X = 260)	6.4	176	[112]
Nanoporous Sb	0.8 M KPF_6	EC:DEC = 1:1 vol%	CMC	71.0	318 (X = 50)	0.5	265	[12]
Sb/CSN	4.0 M KTFSI	EC:DEC = 1:1 vol%	Alginate	61.0	551 (X = 100)	0.2	504	[69]
Sb/C/rGO	0.8 M KFSI	EC:DEC = 1:1 vol%	CMC	46.3	310 (X = 100)	1.5	110	[70]
Sb/NSF-C	5.0 M KFSI	DME	CMC	55.1	363 (X = 200)	1.0	287	[113]
Sb/CNS	1.0 M KPF_6	EC:DMC = 1:1 vol%	CMC	48.0	247 (X = 600)	2.0	101	[114]
Sb/C PNFs	1.0 M KPF_6	EC:DEC = 1:1 vol%	PMMA	71.3	264 (X = 500)	5.0	208	[115]
BiSb/C	5.0 M KFSI	DME	Alginate	70.2	320 (X = 600)	2.0	152	[116]
$Sb_{0.25}Bi_{0.75}$/C	3.0 M KFSI	DME	PVDF	45.0	302 (X = 500)	0.5	276	[117]
Layered Sn-Sb	4.0 M KFSI	EMC	CMC	68.0	296 (X = 150)	5.0	118	[118]
Sb/rGO	0.8 M KPF_6	EC:DEC = 1:1 vol%	CMC	49.3	300 (X = 40)	0.5	210	[119]

Sb-based ASSLIB anodes

Although solid electrolytes provide significant advantages in terms of rigidity, thermal stability, and nonflammability, the direct utilization of Li-metal anodes can induce dendrite formation resulting in short circuits, which remains a critical challenge for ASSLIB development[122]. To address this issue, alloy-based anodes that do not form dendrites have been considered. Lewis *et al.* investigated the critical differences in the SEI layer formation dynamics of LIBs and ASSLIBs, emphasizing the potential benefits of alloy anodes[123]. Due to its immobility, the solid electrolyte in an ASSLIB inhibits excessive SEI layer formation and subsequent electrolyte depletion during continuous cycling. Therefore, alloy-based anodes form mechanically and chemically denser and more stable SEI layers compared to those of LIBs.

Several studies have reported Sb-based anodes for ASSLIBs using oxide- and boride-based solid electrolytes[124-129]. Afyon *et al.* fabricated an Sb composite anode by dropping a slurry of Sb, $Li_{6.25}Al_{0.25}La_3Zr_2O_{12}$ (LLZO), carbon black, and poly(vinylidene fluoride (PVDF) onto the surfaces of LLZO pellets (Sb/LLZO/C) [Figure 15A][124]. The Sb/LLZO/C composite anode exhibited a reversible capacity of 230 mAh g^{-1} with 99.9% retention after 250 cycles at a rate of 240 mA g^{-1} and an operating temperature of 95 °C. This study demonstrated the superior cycling stability and fast rate capability of Sb-based anodes in oxide-type ASSLIBs. Sb-based anodes have predominantly been reported for ASSLIBs that use boride-based solid electrolytes. Mo *et al.* demonstrated that the Sb/$LiBH_4$ solid interfacial contact properties gradually deteriorated owing to the excessive volume change experienced by Sb [Figure 15B][125]. Therefore, a GaSb/$LiBH_4$/C composite anode was designed by introducing liquid Ga metal into the Sb anode to increase interfacial compatibility between the electrode and the solid electrolyte, accommodate volume changes, and promote electron and ion diffusion. The composite anode exhibited a reversible capacity of 400 mAh g^{-1} with a capacity retention of 98.6% after 400 cycles at a current rate of 1 A g^{-1} and an operating temperature of 125 °C. Furthermore, a full-cell employing a TiS_2 cathode and a GaSb/$LiBH_4$/C composite anode delivered a capacity of 226 mAh g^{-1} (based on the mass of GaSb) after 1,000 cycles at a current rate of 0.5 A g^{-1}. Long *et al.* reported the use of liquid Ga metal to induce capacitive behavior and improve the rate capabilities of ASSLIBs [Figure 15C][126]. Liquid Ga was electrochemically introduced from a GaSb anode, and the combination of capacitive behavior and enhanced solid-phase contact was found to promote fast kinetics. The GaSb/$LiBH_4$/C anode demonstrated remarkable cyclability (691 mAh g^{-1} after 800 cycles at a current rate of 660 mA g^{-1}). Kumari *et al.* prepared an Sb/$LiBH_4$/acetylene black (AB) composite that delivered stable cyclability with a reversible capacity of 621 mAh g^{-1} after 50 cycles at a current rate of 150 mA g^{-1}[127]. The buffering effect of $LiBH_4$ and AB on the Sb anode contributed to cycling stability. Sharma *et al.* reported Sb-based chalcogenides, specifically Sb_2X_3 (X = S, Se, or Te), as ASSLIB anodes that use $LiBH_4$ as the solid electrolyte[128]. The prepared Sb_2X_3/$LiBH_4$/AB was evaluated at an operating temperature of 120 °C. While both Sb_2Se_3 and Sb_2Te_3 exhibited poor cyclability owing to excessive volume changes, Sb_2S_3 showed a capacity retention of 80% after 100 cycles. However, all Sb-based chalcogenide anodes exhibited poor ICEs of approximately 50%. Sharma *et al.* also identified a compatible solid electrolyte by changing the solid electrolyte mixed with the anode composite and controlling the operating temperature [Figure 15D][129]. Electrochemical performance was evaluated using $LiBH_4$ as the solid electrolyte at operating temperatures ranging from 40 to 120 °C. The Sb_2S_3/80Li_2S-20P_2S_5 (LPS)/AB composite exhibited a high capacity of 1,373 mAh g^{-1} and high cycling stability (~60% after 100 cycles) at an operating temperature of 120 °C, which is superior to the performance achieved using LPS as the solid electrolyte. Sb-based anodes have been successfully adopted and exhibit high electrochemical performance. To achieve better electrochemical performance of Sb-based anodes for ASSLIBs, further studies focusing on the optimal structure of the Sb-based anode and its compatibility with various solid electrolytes are required. Recent advances in Sb-based anodes for ASSLIBs are summarized in Table 5.

CONCLUSION AND OUTLOOK

Sb is a promising alternative high-performance anode material for use in LIBs, SIBs, PIBs, and ASSLIBs owing to its high theoretical gravimetric and volumetric capacities. However, the significant volume changes experienced by the Sb anode during cycling result in poor cyclability. To address the significant volume-change issue, various strategies based on a complete understanding of the electrochemical reaction mechanisms of Sb anodes have been explored. These strategies include SEI layer control, structural control, and composite/alloy formation.

SEI layer control: Sb-based anodes form unstable SEI layers, which are repeatedly formed and destroyed due to excessive volume changes during cycling. Controlling the composition and structure of the SEI layer is

Table 5. Electrochemical performance of Sb-based ASSLIB anodes

Material	Solid electrolyte	ICE (%)	Cyclability after the Xth cycle (mAh g^{-1})	Rate capability		Ref.
				Current rate (A g^{-1})	Reversible capacity (mAh g^{-1})	
Sb/LLZO/C	$Li_{6.25}Al_{0.25}La_3Zr_2O_{12}$	98.0	230 (X = 240)	0.5	240	[124]
GaSb/$LiBH_4$/C	$LiBH_4$	97.2	400 (X = 400)	6.0	349	[125]
GaSb/$LiBH_4$/C	$LiBH_4$	93.2	691 (X = 800)	3.3	380	[126]
Sb/$LiBH_4$/AB	$LiBH_4$	95.0	621 (X = 50)	-	-	[127]
Sb_2S_3/$LiBH_4$/AB	$LiBH_4$	65.0	448 (X = 100)	-	-	[128]
Sb_2Se_3/$LiBH_4$/AB	$LiBH_4$	68.0	267 (X = 100)	-	-	[128]
Sb_2Te_3/$LiBH_4$/AB	$LiBH_4$	52.0	236 (X = 100)	-	-	[128]
Sb_2S_3/LPS/AB	$LiBH_4$	59.0	774 (X = 100)	-	-	[129]

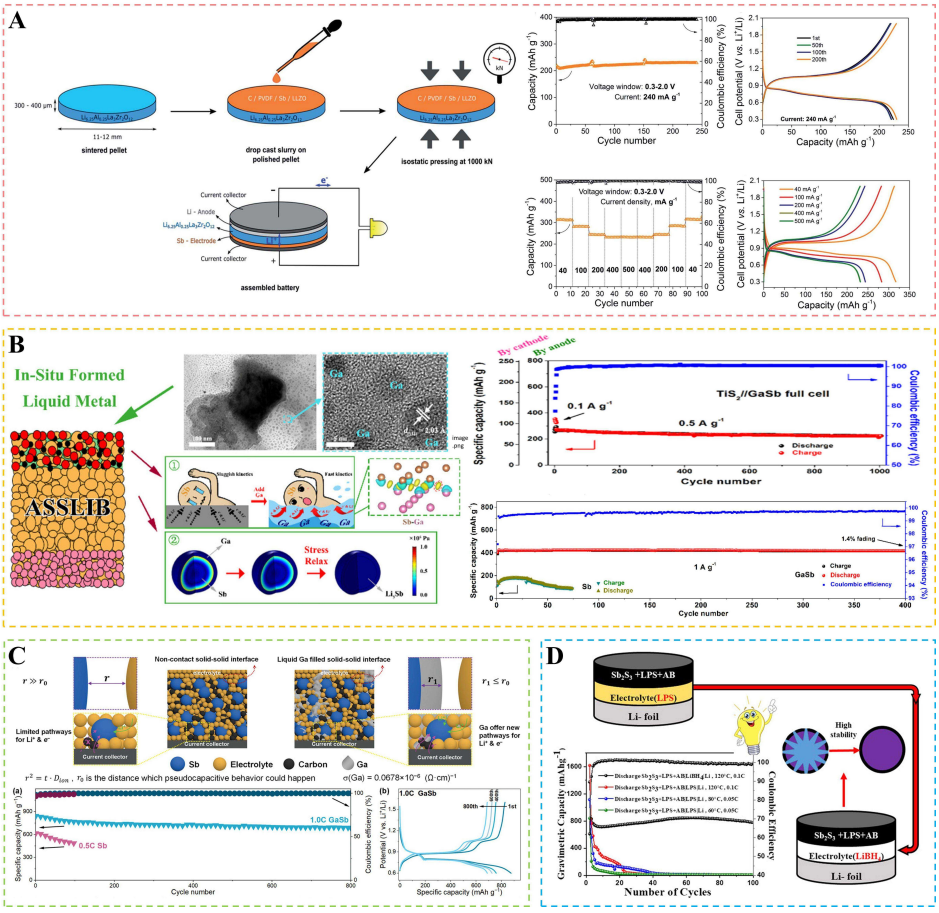

Figure 15. (A) Schematic illustration of an Sb/LLZO/C composite ASSLIB anode[124]. (B) Schematic illustration, TEM images, and cyclability of a GaSb/$LiBH_4$/C composite ASSLIB anode[125]. (C) Schematic illustration and cyclabilities of Sb/$LiBH_4$/C and GaSb/$LiBH_4$/C ASSLIB anodes[126]. (D) Schematic illustration and cyclability of an Sb_2S_3/LPS/AB composite ASSLIB anode[127]. This figure is reproduced with permission from Afyon *et al.*[124], Mo *et al.*[125], Long *et al.*[126], and Kumari *et al.*[127].

crucial for achieving high cycling stability and reversible capacities. Various electrolyte additives provide robust and chemically stable SEI layers. These SEI layer control strategies prevent continuous electrolyte consumption, achieve superior cycling stability, and inhibit side reactions that result in high ICEs and

reversible capacities.

Structural control: Structural control is important for addressing the volume-change issues associated with Sb-based anodes because bulk Sb particles suffer from pulverization owing to large volumetric expansions/contractions. Various multidimensional nanostructures (0D, 1D, 2D, and 3D) provide large surface areas and improve mechanical stability, thereby effectively suppressing and accommodating large volume changes in Sb anodes during cycling. Therefore, structural control of Sb improves cyclability and rate capabilities compared to bulk Sb.

Composite/alloy formation: Sb-based composites and alloys show significant advantages over pristine Sb as anodes for AIBs and ASSLIBs. Incorporating carbon sources into Sb-based composites effectively suppresses the volume change that occurs during repeated cycling, thereby enhancing structural stability. Additionally, the conductive nature of carbon facilitates electron/ion diffusion and contributes to superior cycling stability and high rate capability. In contrast, pristine Sb has low electronic conductivity, leading to rapid capacity degradation and sluggish rate capability. Furthermore, Sb-based alloy materials have been reported to exhibit smaller volume changes during charging and discharging owing to unique reaction mechanisms that involve insertion or conversion reactions.

The abovementioned strategies have led to significant advances in the electrochemical performance of Sb-based anodes for use in LIBs, SIBs, PIBs, and ASSLIBs. The ongoing exploration of innovative strategies is expected to improve the electrochemical performance of Sb-based anodes in terms of cycling stability, rate capability, and reversible capacity. We trust that this review provides a comprehensive insight and guides future research into Sb-based anodes for next-generation battery systems.

DECLARATIONS

Authors' contributions

Writing original draft, content curation, investigation: Yoon JM, Kim DG
Content curation, investigation, writing of review: Kim DH, Lee YH
Conceptualization, validation, visualization, funding acquisition, project administration, supervision, and writing of review and editing: Park CM

Availability of data and materials

Not applicable.

Financial support and sponsorship

This research was supported by Kumoh National Institute of Technology (2022~2024).

Conflicts of interest

Park CM is an Editorial Board member of the journal *Energy Materials*, while the other authors have declared that they have no conflicts of interest.

Ethical approval and consent to participate

Not applicable.

Consent for publication

Not applicable.

REFERENCES

1. Whittingham MS. History, evolution, and future status of energy storage. *Proc IEEE* 2012;100:1518-34. DOI
2. Goodenough JB, Park KS. The Li-ion rechargeable battery: a perspective. *J Am Chem Soc* 2013;135:1167-76. DOI PubMed
3. Tarascon JM, Armand M. Issues and challenges facing rechargeable lithium batteries. *Nature* 2001;414:359-67. DOI PubMed
4. Ding Y, Cano ZP, Yu A, Lu J, Chen Z. Automotive Li-ion batteries: current status and future perspectives. *Electrochem Energy Rev* 2019;2:1-28. DOI
5. Dahn JR, Zheng T, Liu Y, Xue JS. Mechanisms for lithium insertion in carbonaceous materials. *Science* 1995;270:590-3. DOI
6. Palomares V, Casas-cabanas M, Castillo-martínez E, Han MH, Rojo T. Update on Na-based battery materials. A growing research path. *Energy Environ Sci* 2013;6:2312. DOI
7. Palomares V, Serras P, Villaluenga I, Hueso KB, Carretero-González J, Rojo T. Na-ion batteries, recent advances and present challenges to become low cost energy storage systems. *Energy Environ Sci* 2012;5:5884. DOI
8. Komaba S, Murata W, Ishikawa T, et al. Electrochemical Na insertion and solid electrolyte interphase for hard-carbon electrodes and application to Na-ion batteries. *Adv Funct Mater* 2011;21:3859-67. DOI
9. Imtiaz S, Amiinu IS, Xu Y, Kennedy T, Blackman C, Ryan KM. Progress and perspectives on alloying-type anode materials for advanced potassium-ion batteries. *Mater Today* 2021;48:241-69. DOI
10. Song K, Liu C, Mi L, Chou S, Chen W, Shen C. Recent progress on the alloy-based anode for sodium-ion batteries and potassium-ion batteries. *Small* 2021;17:e1903194. DOI PubMed
11. Sultana I, Rahman MM, Chen Y, Glushenkov AM. Potassium-ion battery anode materials operating through the alloying-dealloying reaction mechanism. *Adv Funct Mater* 2018;28:1703857. DOI
12. An Y, Tian Y, Ci L, Xiong S, Feng J, Qian Y. Micron-sized nanoporous antimony with tunable porosity for high-performance potassium-ion batteries. *ACS Nano* 2018;12:12932-40. DOI
13. Liu Q, Fan L, Ma R, et al. Super long-life potassium-ion batteries based on an antimony@carbon composite anode. *Chem Commun* 2018;54:11773-6. DOI
14. Hwang IS, Lee YH, Yoon JM, Hwa Y, Park CM. GaSb nanocomposite: new high-performance anode material for Na- and K-ion batteries. *Compos Part B Eng* 2022;243:110142. DOI
15. Chen Y, Sun H, Guo J, et al. Research on carbon-based and metal-based negative electrode materials via DFT calculation for high potassium storage performance: a review. *Energy Mater* 2023;3:300044. DOI
16. Fu T, Li PC, He HC, Ding SS, Cai Y, Zhang M. Electrospinning with sulfur powder to prepare CNF@G-Fe_9S_{10} nanofibers with controllable particles distribution for stable potassium-ion storage. *Rare Met* 2023;42:111-21. DOI
17. Finegan DP, Scheel M, Robinson JB, et al. In-operando high-speed tomography of lithium-ion batteries during thermal runaway. *Nat Commun* 2015;6:6924. DOI PubMed PMC
18. Takada K. Solid state batteries with sulfide-based solid electrolytes. *Solid State Ionics* 2004;172:25-30. DOI
19. Yu S, Siegel DJ. Grain boundary softening: a potential mechanism for lithium metal penetration through stiff solid electrolytes. *ACS Appl Mater Inter* 2018;10:38151-8. DOI
20. Lu Y, Zhao CZ, Yuan H, Cheng XB, Huang JQ, Zhang Q. Critical Current density in solid-state lithium metal batteries: mechanism, influences, and strategies. *Adv Funct Mater* 2021;31:2009925. DOI
21. Ohta N, Takada K, Zhang L, Ma R, Osada M, Sasaki T. Enhancement of the high-rate capability of solid-state lithium batteries by nanoscale interfacial modification. *Adv Mater* 2006;18:2226-9. DOI
22. Xia X, Dahn JR. Study of the reactivity of Na/hard carbon with different solvents and electrolytes. *J Electrochem Soc* 2012;159:A515-9. DOI
23. Stevens DA, Dahn JR. The mechanisms of lithium and sodium insertion in carbon materials. *J Electrochem Soc* 2001;148:A803. DOI
24. Irisarri E, Ponrouch A, Palacin MR. Review - hard carbon negative electrode materials for sodium-ion batteries. *J Electrochem Soc* 2015;162:A2476-82. DOI
25. Takada K, Inada T, Kajiyama A, et al. Solid-state lithium battery with graphite anode. *Solid State Ionics* 2003;158:269-74. DOI
26. Höltschi L, Borca CN, Huthwelker T, et al. Performance-limiting factors of graphite in sulfide-based all-solid-state lithium-ion batteries. *Electrochim Acta* 2021;389:138735. DOI
27. Park CM, Kim JH, Kim H, Sohn HJ. Li-alloy based anode materials for Li secondary batteries. *Chem Soc Rev* 2010;39:3115-41. DOI PubMed
28. Liu N, Li W, Pasta M, Cui Y. Nanomaterials for electrochemical energy storage. *Front Phys* 2014;9:323-50. DOI
29. Obrovac MN, Chevrier VL. Alloy negative electrodes for Li-ion batteries. *Chem Rev* 2014;114:11444-502. DOI PubMed
30. Nam KH, Park CM. Layered Sb_2Te_3 and its nanocomposite: a new and outstanding electrode material for superior rechargeable Li-ion batteries. *J Mater Chem A* 2016;4:8562-5. DOI
31. Hwang IS, Lee YH, Ganesan V, Hwa Y, Park CM. High-energy-density gallium antimonide compound anode and optimized nanocomposite fabrication route for Li-ion batteries. *ACS Appl Energy Mater* 2022;5:8940-51. DOI

32. Tian H, Tian H, Wang S, et al. High-power lithium-selenium batteries enabled by atomic cobalt electrocatalyst in hollow carbon cathode. *Nat Commun* 2020;11:5025. DOI PubMed PMC
33. Park CM, Sohn HJ. Quasi-intercalation and facile amorphization in layered ZnSb for Li-ion batteries. *Adv Mater* 2010;22:47-52. DOI PubMed
34. Park CM, Sohn HJ. Novel antimony/aluminum/carbon nanocomposite for high-performance rechargeable lithium batteries. *Chem Mater* 2008;20:3169-73. DOI
35. Zhao Q, Meng Y, Su L, Cen W, Wang Q, Xiao D. Nitrogen/oxygen codoped hierarchical porous Carbons/Selenium cathode with excellent lithium and sodium storage behavior. *J Colloid Interface Sci* 2022;608:265-74. DOI
36. He B, Feng L, Hong G, et al. A generic F-doped strategy for biomass hard carbon to achieve fast and stable kinetics in sodium/potassium-ion batteries. *Chem Eng J* 2024;490:151636. DOI
37. Sung JH, Park CM. Amorphized Sb-based composite for high-performance Li-ion battery anodes. *J Electroanal Chem* 2013;700:12-6. DOI
38. Sung JH, Park CM. Sb-based nanostructured composite with embedded TiO_2 for Li-ion battery anodes. *Mater Lett* 2013;98:15-8. DOI
39. Chen X, Mu Y, Liao Z, et al. Advancing high-performance one-dimensional Si/carbon anodes: current status and challenges. *Carbon Neutral* 2024;3:199-221. DOI
40. Ying H, Han WQ. Metallic Sn-based anode materials: application in high-performance lithium-ion and sodium-ion batteries. *Adv Sci* 2017;4:1700298. DOI PubMed PMC
41. Wang A, Kadam S, Li H, Shi S, Qi Y. Review on modeling of the anode solid electrolyte interphase (SEI) for lithium-ion batteries. *NPJ Comput Mater* 2018;4:15. DOI
42. He M, Kravchyk K, Walter M, Kovalenko MV. Monodisperse antimony nanocrystals for high-rate Li-ion and Na-ion battery anodes: nano versus bulk. *Nano Lett* 2014;14:1255-62. DOI PubMed
43. Park CM, Jeon KJ. Porous structured SnSb/C nanocomposites for Li-ion battery anodes. *Chem Commun* 2011;47:2122-4. DOI PubMed
44. Nam KH, Park CM. 2D layered Sb_2Se_3-based amorphous composite for high-performance Li- and Na-ion battery anodes. *J Power Sources* 2019;433:126639. DOI
45. Choi JH, Ha CW, Choi HY, Seong JW, Park CM, Lee SM. Porous carbon-free SnSb anodes for high-performance Na-ion batteries. *J Power Sources* 2018;386:34-9. DOI
46. Park CM, Sohn HJ. A mechano- and electrochemically controlled SnSb/C nanocomposite for rechargeable Li-ion batteries. *Electrochim Acta* 2009;54:6367-73. DOI
47. Park MG, Song JH, Sohn JS, Lee CK, Park CM. Co-Sb intermetallic compounds and their disproportionated nanocomposites as high-performance anodes for rechargeable Li-ion batteries. *J Mater Chem A* 2014;2:11391-9. DOI
48. Park CM, Sohn HJ. Electrochemical Characteristics of $TiSb_2$ and Sb/TiC/C nanocomposites as anodes for rechargeable Li-ion batteries. *J Electrochem Soc* 2010;157:A46. DOI
49. Liu D, Liu ZJ, Li X, et al. Group IVA element (Si, Ge, Sn)-based alloying/dealloying anodes as negative electrodes for full-cell lithium-ion batteries. *Small* 2017;13:1702000. DOI
50. Park CM, Sohn HJ. Antimonides ($FeSb_2$, $CrSb_2$) with orthorhombic structure and their nanocomposites for rechargeable Li-ion batteries. *Electrochim Acta* 2010;55:4987-94. DOI
51. Seo JU, Park CM. Nanostructured SnSb/MOx (M = Al or Mg)/C composites: hybrid mechanochemical synthesis and excellent Li storage performances. *J Mater Chem A* 2013;1:15316. DOI
52. Li H, Yamaguchi T, Matsumoto S, et al. Circumventing huge volume strain in alloy anodes of lithium batteries. *Nat Commun* 2020;11:1584. DOI PubMed PMC
53. Park CM, Hwa Y, Sung NE, Sohn HJ. Stibnite (Sb_2S_3) and its amorphous composite as dual electrodes for rechargeable lithium batteries. *J Mater Chem* 2010;20:1097-102. DOI
54. Jang YH, Park CM. High-performance CoSbS-based Na-ion battery anodes. *Mater Today Energy* 2020;17:100470. DOI
55. Wang F, Chen G, Zhang N, Liu X, Ma R. Engineering of carbon and other protective coating layers for stabilizing silicon anode materials. *Carbon Energy* 2019;1:219-45. DOI
56. Meng W, Guo M, Cheng L, Bai Z, Yang F. Effect of polypyrrole coating on lithium storage for hollow Sb microspheres. *J Electron Mater* 2019;48:2233-41. DOI
57. Gabaudan V, Touja J, Cot D, Flahaut E, Stievano L, Monconduit L. Double-walled carbon nanotubes, a performing additive to enhance capacity retention of antimony anode in potassium-ion batteries. *Electrochem Commun* 2019;105:106493. DOI
58. Pfeifer K, Arnold S, Budak Ö, et al. Choosing the right carbon additive is of vital importance for high-performance Sb-based Na-ion batteries. *J Mater Chem A* 2020;8:6092-104. DOI
59. Wang S, Lee PK, Yang X, Rogach AL, Armstrong AR, Yu DYW. Polyimide-cellulose interaction in Sb anode enables fast charging lithium-ion battery application. *Mater Today Energy* 2018;9:295-302. DOI
60. Park CM, Yoon S, Lee SI, Kim JH, Jung J, Sohn HJ. High-rate capability and enhanced cyclability of antimony-based composites for lithium rechargeable batteries. *J Electrochem Soc* 2007;154:A917. DOI
61. Shin J, Kim S, Park H, Won Jang H, Cahill DG, Braun PV. Thermal conductivity of intercalation, conversion, and alloying lithium-ion battery electrode materials as function of their state of charge. *Curr Opin Solid St Mater Sci* 2022;26:100980. DOI

62. Chang D, Huo H, Johnston KE, et al. Elucidating the origins of phase transformation hysteresis during electrochemical cycling of Li-Sb electrodes. *J Mater Chem A* 2015;3:18928-43. DOI
63. Darwiche A, Marino C, Sougrati MT, Fraisse B, Stievano L, Monconduit L. Better cycling performances of bulk Sb in Na-ion batteries compared to Li-ion systems: an unexpected electrochemical mechanism. *J Am Chem Soc* 2012;134:20805-11. DOI PubMed
64. Caputo R. An insight into sodiation of antimony from first-principles crystal structure prediction. *J Electron Mater* 2016;45:999-1010. DOI
65. Yu S, Zhang X, Zhang P. Prediction of new structures of the Na-Sb alloy anode for Na-ion batteries. *J Phys Chem C* 2022;126:11468-74. DOI
66. Yu DK, Park CM. Sb-based intermetallics and nanocomposites as stable and fast Na-ion battery anodes. *Chem Eng J* 2021;409:127380. DOI
67. Tian W, Zhang S, Huo C, et al. Few-layer antimonene: anisotropic expansion and reversible crystalline-phase evolution enable large-capacity and long-life Na-ion batteries. *ACS Nano* 2018;12:1887-93. DOI
68. Gabaudan V, Berthelot R, Stievano L, Monconduit L. Inside the alloy mechanism of Sb and Bi electrodes for K-ion batteries. *J Phys Chem C* 2018;122:18266-73. DOI
69. Zheng J, Yang Y, Fan X, et al. Extremely stable antimony-carbon composite anodes for potassium-ion batteries. *Energy Environ Sci* 2019;12:615-23. DOI
70. Ko YN, Choi SH, Kim H, Kim HJ. One-pot formation of Sb-carbon microspheres with graphene sheets: potassium-ion storage properties and discharge mechanisms. *ACS Appl Mater Interfaces* 2019;11:27973-81. DOI PubMed
71. Xu K. Electrolytes and interphases in Li-ion batteries and beyond. *Chem Rev* 2014;114:11503-618. DOI PubMed
72. Bian X, Dong Y, Zhao D, et al. Microsized antimony as a stable anode in fluoroethylene carbonate containing electrolytes for rechargeable lithium-/sodium-ion batteries. *ACS Appl Mater Interfaces* 2020;12:3554-62. DOI
73. Sun Q, Cao Z, Ma Z, et al. Dipole-dipole interaction induced electrolyte interfacial model to stabilize antimony anode for high-safety lithium-ion batteries. *ACS Energy Lett* 2022;7:3545-56. DOI
74. Cai T, Sun Q, Cao Z, et al. Electrolyte additive-controlled interfacial models enabling stable antimony anodes for lithium-ion batteries. *J Phys Chem C* 2022;126:20302-13. DOI
75. Liu X, Tian Y, Cao X, et al. Aerosol-assisted synthesis of spherical Sb/C composites as advanced anodes for lithium ion and sodium ion batteries. *ACS Appl Energy Mater* 2018;1:6381-7. DOI
76. Schulze MC, Belson RM, Kraynak LA, Prieto AL. Electrodeposition of Sb/CNT composite films as anodes for Li- and Na-ion batteries. *Energy Stor Mater* 2020;25:572-84. DOI
77. Luo W, Li F, Gaumet J, et al. Bottom-up confined synthesis of nanorod-in-nanotube structured Sb@N-C for durable lithium and sodium storage. *Adv Energy Mater* 2018;8:1703237. DOI
78. Zhang X, Lai F, Chen Z, He X, Li Q, Wang H. Metallic Sb nanoparticles embedded in carbon nanosheets as anode material for lithium ion batteries with superior rate capability and long cycling stability. *Electrochim Acta* 2018;283:1689-94. DOI
79. Pan Q, Wu Y, Zheng F, et al. Facile synthesis of M-Sb (M = Ni, Sn) alloy nanoparticles embedded in N-doped carbon nanosheets as high performance anode materials for lithium ion batteries. *Chem Eng J* 2018;348:653-60. DOI
80. Yu L, Zhang L, Fu J, Yun J, Kim KH. Hierarchical tiny-Sb encapsulated in MOFs derived-carbon and TiO_2 hollow nanotubes for enhanced Li/Na-Ion half-and full-cell batteries. *Chem Eng J* 2021;417:129106. DOI
81. Yang T, Zhong J, Liu J, et al. A general strategy for antimony-based alloy nanocomposite embedded in swiss-cheese-like nitrogen-doped porous carbon for energy storage. *Adv Funct Mater* 2021;31:2009433. DOI
82. Coquil G, Fraisse B, Biscaglia S, Aymé-perrot D, Sougrati MT, Monconduit L. $ZnSnSb_2$ anode: a solid solution behavior enabling high rate capability in Li-ion batteries. *J Power Sources* 2019;441:227165. DOI
83. Su M, Li J, He K, et al. NiSb/nitrogen-doped carbon derived from Ni-based framework as advanced anode for lithium-ion batteries. *J Colloid Interface Sci* 2023;629:83-91. DOI
84. Pan Q, Wu Y, Zhong W, et al. Carbon nanosheets encapsulated NiSb nanoparticles as advanced anode materials for lithium-ion batteries. *Energy Environ Mater* 2020;3:186-91. DOI
85. Yin W, Chai W, Wang K, Ye W, Rui Y, Tang B. Facile synthesis of Sb nanoparticles anchored on reduced graphene oxides as excellent anode materials for lithium-ion batteries. *J Alloy Compd* 2019;797:1249-57. DOI
86. Wang H, Yang X, Wu Q, et al. Encapsulating silica/antimony into porous electrospun carbon nanofibers with robust structure stability for high-efficiency lithium storage. *ACS Nano* 2018;12:3406-16. DOI
87. Lee JO, Seo JU, Song JH, Park CM, Lee CK. Electrochemical characteristics of ternary compound CoSbS for application in Li secondary batteries. *Electrochem Commun* 2013;28:71-4. DOI
88. Park MG, Lee CK, Park CM. Amorphized ZnSb-based composite anodes for high-performance Li-ion batteries. *RSC Adv* 2014;4:5830. DOI
89. Lu H, Wu L, Xiao L, Ai X, Yang H, Cao Y. Investigation of the effect of fluoroethylene carbonate additive on electrochemical performance of Sb-based anode for sodium-ion batteries. *Electrochim Acta* 2016;190:402-8. DOI
90. Bodenes L, Darwiche A, Monconduit L, Martinez H. The solid electrolyte interphase a key parameter of the high performance of Sb in sodium-ion batteries: comparative X-ray photoelectron spectroscopy study of Sb/Na-ion and Sb/Li-ion batteries. *J Power Sources* 2015;273:14-24. DOI

91. Liu Y, Zhou B, Liu S, Ma Q, Zhang WH. Galvanic replacement synthesis of highly uniform Sb nanotubes: reaction mechanism and enhanced sodium storage performance. *ACS Nano* 2019;13:5885-92. DOI
92. Liu Y, Qing Y, Zhou B, et al. Yolk-shell Sb@Void@Graphdiyne nanoboxes for high-rate and long cycle life sodium-ion batteries. *ACS Nano* 2023;17:2431-9. DOI
93. Li P, Yu L, Ji S, et al. Facile synthesis of three-dimensional porous interconnected carbon matrix embedded with Sb nanoparticles as superior anode for Na-ion batteries. *Chem Eng J* 2019;374:502-10. DOI
94. Chen B, Qin H, Li K, et al. Yolk-shelled Sb@C nanoconfined nitrogen/sulfur co-doped 3D porous carbon microspheres for sodium-ion battery anode with ultralong high-rate cycling. *Nano Energy* 2019;66:104133. DOI
95. Li H, Wang K, Zhou M, et al. Facile tailoring of multidimensional nanostructured Sb for sodium storage applications. *ACS Nano* 2019;13:9533-40. DOI
96. Yang Y, Shi W, Leng S, Cheng H. Multidimensional antimony nanomaterials tailored by electrochemical engineering for advanced sodium-ion and potassium-ion batteries. *J Colloid Interface Sci* 2022;628:41-52. DOI PubMed
97. Ma W, Wang J, Gao H, et al. A mesoporous antimony-based nanocomposite for advanced sodium ion batteries. *Energy Stor Mater* 2018;13:247-56. DOI
98. Xie M, Li C, Ren S, et al. Ultrafine Sb nanoparticles *in situ* confined in covalent organic frameworks for high-performance sodium-ion battery anodes. *J Mater Chem A* 2022;10:15089-100. DOI
99. Zheng X, You J, Fan J, et al. Electrodeposited binder-free Sb/NiSb anode of sodium-ion batteries with excellent cycle stability and rate capability and new insights into its reaction mechanism by operando XRD analysis. *Nano Energy* 2020;77:105123. DOI
100. Ma W, Yin K, Gao H, Niu J, Peng Z, Zhang Z. Alloying boosting superior sodium storage performance in nanoporous tin-antimony alloy anode for sodium ion batteries. *Nano Energy* 2018;54:349-59. DOI
101. Gao H, Niu J, Zhang C, et al. A dealloying synthetic strategy for nanoporous bismuth-antimony anodes for sodium ion batteries. *ACS Nano* 2018;12:3568-77. DOI
102. Pan J, Yu K, Mao H, et al. Crystalline Sb or Bi in amorphous Ti-based oxides as anode materials for sodium storage. *Chem Eng J* 2020;380:122624. DOI
103. Choi JH, Ha CW, Choi HY, et al. Sb_2S_3 embedded in amorphous P/C composite matrix as high-performance anode material for sodium ion batteries. *Electrochim Acta* 2016;210:588-95. DOI
104. Nam KH, Choi JH, Park CM. Highly reversible Na-ion reaction in nanostructured Sb_2Te_3-C composites as Na-ion battery anodes. *J Electrochem Soc* 2017;164:A2056-64. DOI
105. Zhang Q, Mao J, Pang WK, et al. Boosting the potassium storage performance of alloy-based anode materials via electrolyte salt chemistry. *Adv Energy Mater* 2018;8:1703288. DOI
106. Zhou L, Cao Z, Zhang J, et al. Electrolyte-mediated stabilization of high-capacity micro-sized antimony anodes for potassium-ion batteries. *Adv Mater* 2021;33:2005993. DOI
107. Du X, Gao Y, Zhang B. Building elastic solid electrolyte interphases for stabilizing microsized antimony anodes in potassium ion batteries. *Adv Funct Mater* 2021;31:2102562. DOI
108. Shi Y, Wang L, Zhou D, Wu T, Xiao Z. A flower-like $Sb_4O_5Cl_2$ cluster-based material as anode for potassium ion batteries. *Appl Surf Sci* 2022;583:152509. DOI
109. Liu X, Zhu J, Yue L, et al. Green and scalable template-free strategy to fabricate honeycomb-like interconnected porous micro-sized layered Sb for high-performance potassium storage. *Small* 2022;18:2204552. DOI
110. Imtiaz S, Kapuria N, Amiinu IS, et al. Directly deposited antimony on a copper silicide nanowire array as a high-performance potassium-ion battery anode with a long cycle life. *Adv Funct Mater* 2023;33:2209566. DOI
111. Guo X, Gao H, Wang S, et al. MXene-based aerogel anchored with antimony single atoms and quantum dots for high-performance potassium-ion batteries. *Nano Lett* 2022;22:1225-32. DOI
112. He X, Liu Z, Liao J, et al. A three-dimensional macroporous antimony@carbon composite as a high-performance anode material for potassium-ion batteries. *J Mater Chem A* 2019;7:9629-37. DOI
113. Shi X, Liu W, Zhao S, et al. Integrated anodes from heteroatoms (N, S, and F) co-doping antimony/carbon composite for efficient alkaline ion (Li^+/K^+) storage. *ACS Appl Energy Mater* 2022;5:12925-36. DOI
114. Han Y, Li T, Li Y, et al. Stabilizing antimony nanocrystals within ultrathin carbon nanosheets for high-performance K-ion storage. *Energy Stor Mater* 2019;20:46-54. DOI
115. Cao K, Liu H, Jia Y, et al. Flexible antimony@carbon integrated anode for high-performance potassium-ion battery. *Adv Mater Technol* 2020;5:2000199. DOI
116. Xiong P, Wu J, Zhou M, Xu Y. Bismuth-antimony alloy nanoparticle@porous carbon nanosheet composite anode for high-performance potassium-ion batteries. *ACS Nano* 2020;14:1018-26. DOI
117. Liu J, Zhang D, Cui J, et al. Construction of the fast potassiation path in Sb_xBi_{1-x}@NC anode with ultrahigh cycling stability for potassium-ion batteries. *Small* 2023;19:2301444. DOI
118. Ding H, Wang J, Fan L, et al. Sn-Sb compounds with novel structure for stable potassium storage. *Chem Eng J* 2020;395:125147. DOI
119. Yi Z, Lin N, Zhang W, Wang W, Zhu Y, Qian Y. Preparation of Sb nanoparticles in molten salt and their potassium storage performance and mechanism. *Nanoscale* 2018;10:13236-41. DOI PubMed
120. Baek S, Jie S, Lee B. Effects of fluoroethylene carbonate additive on potassium metal anode. *J Mech Sci Technol* 2023;37:3657-65.

DOI

121. Yoon SU, Kim H, Jin HJ, Yun YS. Effects of fluoroethylene carbonate-induced solid-electrolyte-interface layers on carbon-based anode materials for potassium ion batteries. *Appl Surf Sci* 2021;547:149193. DOI
122. Wang S, Wu Y, Ma T, Chen L, Li H, Wu F. Thermal stability between sulfide solid electrolytes and oxide cathode. *ACS Nano* 2022;16:16158-76. DOI
123. Lewis JA, Cavallaro KA, Liu Y, Mcdowell MT. The promise of alloy anodes for solid-state batteries. *Joule* 2022;6:1418-30. DOI
124. Afyon S, Kravchyk KV, Wang S, et al. Building better all-solid-state batteries with Li-garnet solid electrolytes and metalloid anodes. *J Mater Chem A* 2019;7:21299-308. DOI
125. Mo F, Ruan J, Fu W, et al. Revealing the role of liquid metals at the anode-electrolyte interface for all solid-state lithium-ion batteries. *ACS Appl Mater Interfaces* 2020;12:38232-40. DOI
126. Long Z, Ruan J, Li S, et al. Could capacitive behavior be triggered in inorganic electrolyte-based all-solid-state batteries? *Adv Funct Mater* 2022;32:2205667. DOI
127. Kumari P, Sharma K, Pal P, Kumar M, Ichikawa T, Jain A. Highly efficient & stable Bi & Sb anodes using lithium borohydride as solid electrolyte in Li-ion batteries. *RSC Adv* 2019;9:13077-81. DOI PubMed PMC
128. Sharma K, Singh R, Ichikawa T, Kumar M, Jain A. Lithiation mechanism of antimony chalcogenides (Sb_2X_3; X = S, Se, Te) electrodes for high-capacity all-solid-state Li-ion battery. *Int J Energy Res* 2021;45:11135-45. DOI
129. Sharma K, Singh R, Tripathi B, Ichikawa T, Kumar M, Jain A. All-solid-state Li-ion batteries using a combination of Sb_2S_3/Li_2S-P_2S_5 /acetylene black as the electrode composite and $LiBH_4$ as the electrolyte. *ACS Appl Energy Mater* 2021;4:6269-76. DOI